José Rui Gaspar da Silva

Bachelor in Micro and Nanotechnologies Engineering

Study on the viability of a 4x2 HEB mixer array at super-THz based on a Fourier phase grating LO for space applications

Dissertation submitted in partial fulfillment
of the requirements for the degree of

Master of Science in
Micro and Nanotechnologies Engineering

Adviser: Dr. Darren Hayton, Instrument Scientist, Netherlands Institute for Space Research

Co-advisers: Dr. Jian - Rong Gao, Senior Instrument Scientist, Netherlands Institute for Space Research

Dr. Rodrigo Paiva Fernão Martins, Full Professor, Faculty of Sciences and Technology, NOVA University of Lisbon

Examination Committee

Chairperson: Dr. Hugo Manuel Brito Águas
Raporteurs: Dr. João Carlos da Palma Goes
Dr. Jian-Rong Gao

FACULDADE DE CIÊNCIAS E TECNOLOGIA
UNIVERSIDADE NOVA DE LISBOA

September, 2016

Study on the viability of a 4x2 HEB mixer array at super-THz based on a Fourier phase grating LO for space applications

This document was created using the (pdf)LaTeX processor, based in the "unlthesis" template[1], developed at the Dep. Informática of FCT-NOVA [2].
[1] https://github.com/joaomlourenco/unlthesis [2] http://www.di.fct.unl.pt

And AC said: "LET THERE BE LIGHT".
And there was light

"The Last Question", Isaac Asimov

Acknowledgements

In this section I would like to acknowledge all the people that somehow made a difference throughout the last 5 years and helped shape the person that I'm today. A big thank you to all.

Firstly I would like to thank my coordinator, Dr. Darren Hayton. There aren't words that can even start to describe all the support that he has provide me during my work at SRON. Thanks to his guidance and support it was easy to tackle all the challenges that this work presented. He surely will serve as an inspiration for my life. You started as a coordinator, and ended as a friend. Thank you.

A very special thanks to Dr. Jian Gao for accepting me into this project, and mainly to have me redirected into SRON. Without you I wouldn't be able to fulfill an old dream of working in space related research. I would also like to thank you for all the insights, availability and discussions during my stay, and as well the trust you put on me for the future.

Um agradecimento especial ao meu orientador na FCT, o Prof. Dr. Rodrigo Martins, não só pelo apoio durante esta tese mas também pelo apoio nas diversas aventuras partilhadas ao longo dos anos. Destaco o IV Encontro Nacional de Estudante de Materiais, o qual sem o seu apoio nunca teria tido tanto sucesso. Obrigado ainda pela confiança demonstrada em mim ao longo dos anos.

I would like to acknowledge SRON for receiving me, and specially to all SRON-Groningen staff without whom this thesis would have not been possible. A big thanks to Koen and his amazing vocal skills to motivate me through "Write your thesis" using the GoT theme song, you are a really nice guy! A special thanks to Willem-Jan which was crucial in my experience with the bond-wiring machine. If I'm Mr. Bond, you are my M.

To Behnam Mirzaei, PHD student at TU Delft, for all the amazing work on the grating design and simulations, and also for all the help and discussions regarding the grating the characterization.

A toda à minha família, e em especial aos meus pais, irmãos, cunhada e sobrinho por todo o apoio incondicional que demonstraram durante este tempo lá fora. Que saibam que vos tive sempre no pensamento. Obrigado tanto pelo apoio, como pelas video-chamadas, que ajudaram a encurtar a distância. Obrigado ainda por confiarem em mim neste nova etapa que se avizinha.

Ao Ricardo Farinha, que comigo partilhou esta aventura por terras holandesas. Obrigado por teres vivido comigo estes últimos meses por lá, pelas discussões infinitas e opiniões, pela aleatoriedade natural que te persegue e é contagiante. Obrigado.

A todo o corpo docente do DCM, em especial ao Prof. Rodrigo Martins e à Prof. Elvira Fortunato sem os quais este curso não existiria. Um agradecimento também aos professores Luis Pereira, Pedro Barquinha, Isabel Ferreira, Rui Igreja e Guilherme Lavareda que sinto que de alguma forma tiveram um impacto especial na minha formação.

À professora Ana Luísa Custódio, por ter instigado a minha paixão pela matemática tanto através do SIAM Student Chapter, como pela optimização sem derivadas. Mais que uma professora, uma amiga que levarei comigo para a vida. Ao SIAM student Chapter, por provarmos que afinal a matemática não é só para matemáticos. Uma pequena grande família.

Ao Angelo santos, por todas as conversas, discussões, fritanços, e aquele teamwork quando mais importava. Não és apenas um grande amigo, és um irmão, podia estar aqui com muitas coisas mas sabes o que sinto. Também ao José Rosa, que juntamente com o angelo fecha aqui

os três mosqueteiros da nanotecnologia. Obrigado por teres uma visão tão diferente da vida, é inspiradora.

Às damas do meu nano baralho: Ana gaspar, Andreia neto, Filipa Fernandes e Sofia chamiço. Por todos os trabalhos em conjunto, todas as festas, conversas, e momentos fenomenais. Serão sempre as damas mais importantes. Um agradecimento especial à Ana por todas a unhas ruidas comigo nas ultimas etapas deste percurso, bem como pelas noites de conversa. Que as garrafas de verde nunca se acabem.

À Sofia Martins porque se existem damas, também temos Jokers. Por nunca teres perdido esse sotaque nortenho, nem mudares a tua forma de ser desde o início. Obrigado pelo apoio mental e por me mostrares que existe algo mais que a 202 na vida, crescemos muito juntos.

À minha BRIS! Amorim, obrigado por tudo... e tudo é mesmo muita coisa. Das amizades mais improváveis que levo comigo para a vida. Podia estar com muitas coisas mas tu sabes o que sinto BRIS. À Marina Teixeira pelos anos de amizade e partilha de momentos, obrigado por tudo. Ao pessoal do monte, Miguel, Tiago, Mário, Raquel, Boiça, Pacotes, Catarina. Trouxeram aos meus ultimos anos excelentes momentos, momentos esses que estarão para sempre na minha memória.

Ao Alex "Panda" Grüninger. Não tenho muitas palavras para descrever a admiração que tenho para ti. Foste uma das minhas maiores inspiração neste curso, e extrai de ti o fantástico espirito de sacrifício e de "noção" que tanta falta faz a tanta gente. À Rita Pontes, por todas as conversas, conselhos de moda, carolos e etc's, és grande! À Susana Marques, por me mostrar que mesmo pessoas com mau feitio podem ser boas amigas. Ao Trofas, pela amizade, pelos conselhos, e pequenas aventuras, tu vais longe. À Catarina Rodrigues e ao Rambo, por terem estado sempre lá quando era preciso. Um especial obrigado à Alexandra Loupas, por seres quem és. Ao Ricardo Ramos pelas conversas infindáveis, ajuda incondicional e companheirismo à distância. Ao Gonçalo Santos, por todos os vacilanços que passamos juntos. Ao Tiago Rosado, mais uma amizade improvável, capaz de me mostrar que existe todo um mundo lá fora, obrigado ainda por todos os conselhos.

Ao pessoal do monte, Miguel, Tiago, Mário, Raquel, Boiça, Pacotes, Catarina. Trouxeram aos meus ultimos anos excelentes momentos, momentos esses que estarão para sempre na minha memória. Também ao pessoal de nano que me acompanharam ao longo de todos os anos, e fizeram da minha vida algo muito mais feliz. Um agradecimento especial à 202. Um agradecimento especial a todos os meus alunos, espero que vos tenha transmitido um pouco mais do que apenas matéria.

Aos meus afilhados, Cunha, Viorel, Tiago, Gonçalo, Filipe, Mafalda, Catarina, Ramos e Maria Helena. Tentei ser um exemplo a seguir e espero ter conseguido, mas também aprendi muito com vocês. Boa sorte e contem sempre comigo.

Ao Pedro Salomé do INL, ainda que a minha estadia tenha sido curta, tiveste um impacto gigante na forma como passei a olhar a vida e o mundo da investigação. A tua personalidade e atitude perante o mundo é inspiradora.

À Sara Oliveira e à Sónia Seixas. Obrigado pelo ENEM, pelas Jortecs e eventos aleatórios, mas também simplesmente por serem quem são, fantásticas. "Boa noite".

A toda o grupo da Elite, obrigado por estarem sempre lá nem que fosse para me mostrarem o que eu andava a perder em ansião. Foram uma peça chave ao longo destes últimos anos para que hoje ainda haja uma ligação a Ansião. Ao Pedro Nunes, uma relação que vem desde sempre e que espero que para sempre dure, obrigado por me teres acompanhado até aqui, e ques saibas que podes contar sempre comigo.

To all of my Groninen fam. You made my experience in Groningen so much better. Without you it would have been much boring. A special thanks to Bjorn and Maggie.

Abstract

Various astronomical telescopes including Herschel, ALMA, STO and SOFIA-GREAT have successfully exploited THz radiation in order to explore the cosmos from the birth of the Universe to the life cycle of individual stars. The THz region, however, still remains relatively poorly observed due to poor transmission of THz light through Earth's atmosphere as a result of past technological constraints. One such example is the observation of neutral oxygen [OI] at 4.7 THz which is only now opening up as a possibility for astronomical study.

In this thesis we report on technology development aimed at implementing an advanced 4.7 THz astronomical receiver array for a proposed future NASA balloon mission called GUSTO. Several aspects of the receiver are studied in detail: HEB characterization and selection; Impact of lens size on device sensitivity; LO multiplexing at 1.4 THz using a 4x2 Fourier phase grating as a stepping stone to a 4.7 THz Fourier grating, including a demonstration of a 2x2 pixel array receiver using the central four beams of the grating output beam pattern. Conclusions are presented on the findings that will have direct input to the GUSTO mission.

Keywords: GUSTO, Fourier phase grating, heterodyne, HEB, Instrumentation, Mixer Array, THz

Resumo

Vários telescópios astronómicos como o caso do Herschel, ALMA, STO e o SOFIA-GREAT foram empregues com sucesso no estudo de radiação de THz, com o objetivo de explorar o cosmo desde o nascimento do Universo até ao ciclo de vida das estrelas. A radiação no intervalo dos THz, contudo, continua relativamente pouco estudada devido à sua baixa transmissão através da atmosfera terrestre, para além de limitações ao nível tecnológico. Um exemplo de radiação relevante nesta faixa do espectro prende-se com a observação de moléculas de oxigénio neutro [OI] a 4.7 THz, que apenas recentemente se tornou possível observar para estudos astronómicos

Nesta tese reportamos desenvolvimento tecnológico cujo objetivo último é implementar uma avançada câmara heteródina multipixel, utilizando HEB *mixers*, para observações astronómicas a 4.7 THz para a missão GUSTO proposta à NASA. Diferentes aspetos do *array* são estudados em detalhe: caraterização e seleção de HEBs; Impacto do tamanho das lentes vs sensibilidade; *Multiplexing* de um LO a 1.4 THz usando uma 4x2 Fourier phase grating como prova de conceito para a desejada Fourier grating a 4.7 THz. Neste último, a grating é ainda demonstrada num *array* de 2x2 pixéis utilizando os quatro feixes centrais refletidos pela grating. Apresentam-se conclusões nos resultados que terão impacto direto no desenvolvimento da missão GUSTO.

Palavras-chave: GUSTO, Fourier phase grating, heteródino, HEB, Instrumentação, Mixer Array, THz

v	Frequency
v_{IF}	IF frequency
v_{LO}	LO frequency
ε_{Si}	Silicon dielectric constant, 11.7 at 300 K
v_s	Signal frequency
λ_{th}	Healing distance
$F\#$	Lens focal ratio
I_c	Critical current
P_{opt}	Optimal pumping power
R_N	Normal resistance
T_C	Critical temperature
T_n	Noise temperature
T_{rec}	Receiver noise temperature
h	Planck constant, $6.62607004 \times 10^{-34}\ m^2kg/s$
k_B	Boltzmann constant, $1.38064852 \times 10^{-23}\ m^2kg/s^2K$
[CII]	Ionized Carbon
[NII]	Ionized Nitrogen
[OI]	Neutral Oxygen
NbN	Niobium Nitride

LN_2	liquid nitrogen
AR	anti-reflective
CPW	co-planar waveguide
DSB	double sideband
FFT	fast Fourier transform
FIR	far infrared
GREAT	German receiver for Astronomy at Terahertz
GUSTO	Galactic/X-galactic Ultra long duration ballon Spectroscopic Stratospheric THz Observatory
HDPE	high density poly ethylene
HEB	Hot Electron bolometer
IF	intermediate frequency
KID	Kinetic inductance Detector
LHe	liquid helium
LNA	low noise amplifier
LO	Local Oscillator
QCL	quantum cascade laser
RF	radio frequency
SIS	Superconductor-Insulator-Superconductor
SSB	single sideband
STO	Stratospheric Terahertz Observatory
TES	Transition Edge Sensor

THz Terahertz

Objective

Terahertz radiation is one of the less studied regions of the electromagnetic spectrum, but contains a significant source of information about the cycle of matter in the universe, hence it is crucial for our understanding of how stars with planetary systems came to be. This thesis work is concerned with the viability of developing multipixel heterodyne mixer arrays at super-THz, as a step forward the desired 4.7 THz HEB mixer array for the NASA candidate GUSTO mission, aiming to:

- show that fabrication of detectors (yield) and consistency in performance is sufficiently good that sufficient HEBs can be drawn from the same batch to populate multipixel arrays.
- study how the operation of HEBs is affected by the use of different sized elliptical SI lens in order to achieve smaller dimension array footprint.
- demonstrate capability of dividing a THz beam into 8 at 1.4THz, as a step towards an 8 pixel 4.7 THz receiver for astronomical observations, i.e, GUSTO.
- make suggestions that improve the understanding of gratings and applications of gratings. Transition from 1.4 THz to 4.7 THz is then much more straightforward thanks to this work.

Work structure

To make it easier to understand this work was organized as follows: The motivation introduces the importance of astrophysics missions and in special, the mission where this thesis is included, GUSTO; It is followed by the introduction where it is explained the basics on THz astronomy, detection methods, hot electron bolometers, (being this the crucial sensors for THz detection), the state of the art, and finally the Fourier Phase phase grating, which is the key element for the LO multiplexing. Chapter 2, 3 and 4 describe each of the studies made. Chapter 2 includes all the work done on HEB characterization, introducing first the experimental setup used, and later the results obtained. It includes the characterization and sensor selection process. Chapter 3 introduces the study on lens size vs noise temperature. Here no experimental part is introduced since it's the same as the previous chapter, and therefore only the results of the experiments and simulation are presented. Chapter 4 summarizes all the work done on the Fourier Phase Grating and represents the core of the work of in this thesis. All the optical path designs are presented for the grating characterization and use, it is also described how the data acquisition and treatment was performed. This is followed by the results chapter and the chapter that ends with the demonstration of a 2x2 receiver array. There are also four appendixes added: the first to introduce with more detail the state of the art on this instrumentation field, the second with detailed presentation to the GUSTO mission, a third with the list of all the instruments used in this work and a fourth with full demonstration of the grating equations that can be used in an array design

Where do we come from?

Since antiquity, human curiosity has been sparked by the stars and planets in the night sky, fueling imagination and creating myths. The recordings of sky observations can be traced as far back as the early man's drawings in caves and have since then played an important role in humanity, used to predict future events or as adoration idols. In the last centuries by the hand of big names like Newton, Galileu or Kepler, astronomy saw advances with the invention of telescopes leading to the discovery of far away stars, planets and galaxies. More recently, the race to get space probes into space was another mark in astronomy, allowing for telescopes (such as Hubble) and interplanetary probes to extend even further our ability to explore the space. And all of these efforts with a single quest in mind: to find how we came to be.

Many different missions have been launched in past decades, from stratospheric balloons to satellites. These have allowed Humanity to start unraveling the mysteries behind the cosmos. The GUSTO mission has an ambitious goal of unlocking for the first time a specific line of THz radiation, [OI] at 4.7 THz, that together with the information of other lines already studied, such as [NII] (1.4 THz) and [CII](1.9 THz), can help trace these molecules and therefore allow us to tap into the life cycle of the interstellar clouds, and possible lead us to an understand, for example, of how systems comprised of stars with planets are formed.

Chapter 1

Introduction

1.1 Terahertz Astronomy

Despite all the advances made in astronomy, there are still some regions of the electromagnetic spectrum that remain largely unexplored. One of these regions is the Terahertz (THz), also known as sub-millimeter or far-infrared radiation, defined as a frequency range between 0.3-10 THz (or 30 µm-1 mm wavelength). This region plays a major role in astrophysics since it is the primary source of radiation for the most luminous spectral signatures of ions, atoms and molecules that permeate the Universe. Although the radiation from, e.g. stars, originates mainly in the visible and ultraviolet part of the spectrum, as this radiation interacts with dust in interstellar clouds, it shifts in frequency by reemission in THz or redshift THz emission. Studying this frequency range enables the study of the evolution cycles of matter in galaxies such as the universe carbon cycle (see figure B.1), the life cycle of the Interstellar Medium and also understanding astrophysical phenomena such as cometary atmospheres. All of this leads to understand how the formation of a star with a planetary system happen.[1, 2]

This understanding can be achieved by measuring conditions such as temperature, pressure and dynamics of clouds in galaxies. Temperature and pressure can be obtained with low resolution spectroscopy (coherent detectors), while for dynamic processes, higher spectral resolution provided by heterodynes (indirect detectors) is more favorable. The astronomical application of heterodyne is to use the Doppler shift of a known frequency molecular line to calculate velocity, which require high spectral resolution. The more reliable way to get this data is by studying the Milky Way, where better quality measurements can be performed since other galaxies are too far away to get sufficient spatial resolutions. The data gathered can be used as a template for other galaxies.

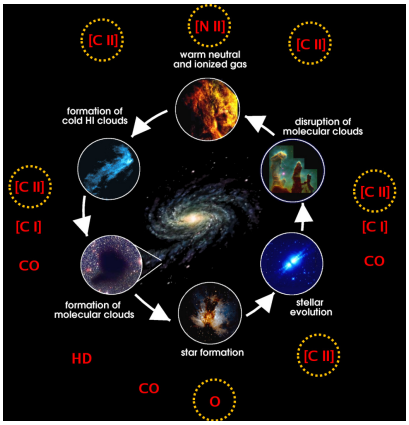

Figure 1.1: Life cycle of interstellar clouds. The cycle starts from the warm neutral and ionized gas formed in hydrogen clouds. It originates molecular clouds that give rise to stars. The stars evolve and by exploding end up again as ionized gas. At each stage we have different molecules (e.g. [CII]) which study can help track this cycle. Adapted from [1]

Difficulties with development of THz sources/detectors and the loss of radiation by absorption from the Earth's atmosphere (mainly due to water vapour), are the key aspects hindering the exploration of this part of the spectrum. Thanks to advancements made in superconducting and quantum technology, it was possible to develop and improve single THz receiver which will be discussed later. Since the sensitivity is finite, it is preferable to make use of the brightest molecular frequency lines available, hence the choice of specific lines to be studied such as, the [NII] (1.4 THz), [CII] (1.9 THz) or [OI] (4.7 THz), being the last hardly studied due to existing technology limitations.

1.2 Detection methods

Detection technologies can be simply divided into two categories: incoherent (direct) or coherent (heterodyne) detection. Despite direct detectors providing superior sensitivities, they are not suited for applications that require ultra-high spectral resolution, which is key to avoid line blending and resolve line shapes of radiation in astronomy. Due to this, heterodyne receivers are generally used for spectroscopy and direct detectors for imaging or low resolution spectroscopy. [3]

1.2.1 Incoherent detection technology

Direct detectors work simply as power detectors, preserving only the signal amplitude information. These type of detectors are considered as broadband detetors. Direct detectors couple all the power received within their sensitive band, they therefore require a band-pass filter or spectrometer at the input in order to avoid undesired frequency detection.[3, 4] Example of direct detectors are the Transition Edge Sensor (TES)[5] and the Kinetic inductance Detector (KID)[6].

1.2.2 Coherent detection technology

In heterodyne detection a mixer is used to down convert a signal at THz into an intermediate frequency (IF), usually around the GHz ($\upsilon_{IF} \ll \upsilon_s$), while preserving both the phase and amplitude information of the original signal. This process (see figure 1.2a) starts by taking an unknown signal and combining it optically with an Local Oscillator (LO) using a beamsplitter/combiner, coupling the combined signal with an antenna/waveguide into the mixer. The mixer will only sense the beat of the optical signal coupled, converting it into an eletrical IF as its output, which accordingly to the mixer theory is known to be: $\upsilon_{IF} = |\upsilon_s - \upsilon_{LO}|$. This frequency transformation allows the signal to be processed by regular radio frequency (RF) electronics. The mixer output is then amplified by the IF amplifier chain, filtered and finally retrieved applying a spectrum analyzer. This produces a spectrometer without any moving parts and with high sensitivity, high spectral resolutions ($\upsilon / \triangle\upsilon \geq 10^7$), but with limited bandwidth. [3]. In the chapter 2 a detailed description of our heterodyne system can be found.

The LO is required to be a signal with an extremely stable phase or frequency that gives the mixer the "tone" with which to mix the target signal and should have enough power to pump the mixer to its optimum operation point. Until recently the main LO sources used have been the FIR gas laser and Schottky diode frequency multiplier, the former being too big to implement in an instrument, and the later losing power exponentially with frequency hence it has only been demonstrated up to 2.7 THz. More recently an alternative laser technology appeared, the quantum cascade laser (QCL)[7], in which promising power output, frequency range and small size lead to its demonstration as effective LO source at 4.7 THz in 2013 [8]. One of the downsides of this technology is the use of cryogenic temperatures.

When using a mixer one should take into account the available LO power, operating temperature and the sensitivity needed, defined as the noise temperature, T_n, of the receiver. A mixer can operate in single sideband (SSB) or in double sideband (DSB) mode. The former is defined as when the mixer outputs two different IF, one for each of the sidebands, while the later only has a single output IF, by which both sidebands are superimposed. The DSB is more

typical at THz frequencies due to its simplicity of construction. The noise levels of both modes are related such that: $T_{SSB} \approx 2T_{DSB}$. [9]

Due to the use of quantum mechanisms in mixers, both phase and amplitude are non-commuting quantities, therefore, based on the Heisenberg Uncertainty Principle, retaining information of both parts is the reason for the existence of a "quantum limit" for mixer sensitivity. This limit, for SSB operation, can be expressed as a noise temperature, $T_n = \frac{h\upsilon}{k_B}$, which is 50K/THz. [9, 10]

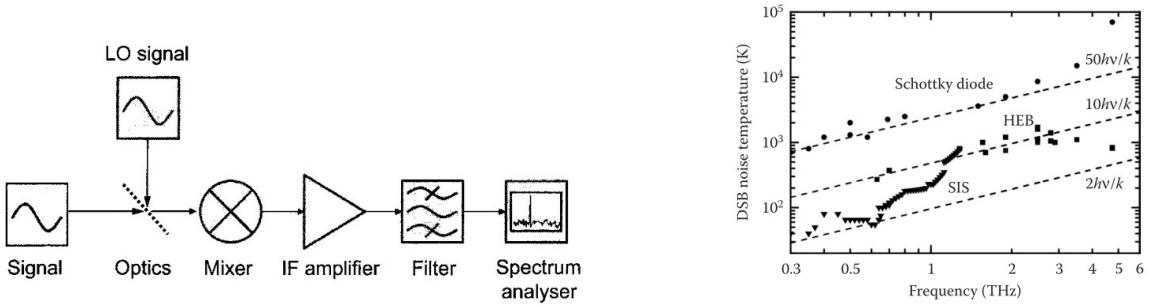

(a) (b)

Figure 1.2: (a) Heterodyne detection scheme. (b) Comparison of measured DSB noise temperatures for heterodyne mixers. The curves for 2, 10 and 50 times the quantum noise limit can be seen. From [9]

There are available different types of mixer for THz detection such as the Superconductor-Insulator-Superconductor (SIS)[11, 12] and the Hot Electron bolometer (HEB) [13, 14], which require cooling to make use of superconducting properties, and the Schottky diodes [15]. Although the later uses semiconductor technology and therefore doesn't have temperature restrictions, is the one that offers the poorest noise temperature and highest requirement for LO power (see figure 1.2b). SIS offers the best sensitivies, but as we move for values higher than 1THz their perfomance deteriorates quickly, hence the HEB being the principal detector at super-THz. [9, 16]

1.3 Hot Electron Bolometers

Hot electron bolometers history starts with Phillips and Jefferts (1973) [13] and later by Gershenzon et al (1990)[14]. These detectors, when used as mixers, are essentially a thin film strip of superconductor material contacted with two normal metal antenna pads. The working principle is the bolometric effect, where small temperature variations due the absorption of incident photons have a strong impact on the resistance of the sensor, and thus is operated in a resistive state. In figure 1.3a the typical IV curve of an HEB is presented. If no DC bias (V_B) is applied to the device, it behaves as a short, increasing its current until a critical value I_C, which is the maximum current output, and marks the end of the superconductive zone (ideally this should happen at 0 V, but in real devices this zone can range within a fraction of a mV where we see a low positive resistance behavior due to resistance of the metal contacts). As the voltage increases, Cooper pairs (pairs of electrons) within the bridge start to break leading the device to stop behaving as a pure superconductor, and resulting in a decrease in current (negative resistance behavior). This is called the non-linear transition region. When the voltage magnitude is high enough, it simply behaves as a normal resistance, hence the name for normal

state region. The operation is based on the combination of the DC bias, LO power and a low bath temperature, T_b (using liquid helium (LHe)), such that it sets the device into the non-linear transition between the superconductive and resistive (normal) state. Since the working principle makes use of hot electrons, from the breaking of cooper pairs, it makes HEB fast enough to act as mixer with reasonable bandwidth. [9]

The mixing in the HEB occurs based on the hot-spot model (see figure 1.3b). When the device is set on the nonlinear transition, the DC dissipation and radiation from the LO heats the bridge creating a zone in the center of the bridge that is in the normal state, referred also as the hot-spot, and has a length L_H in figure 1.3b. Heating due to the absorption of the target signal and LO causes L_H to be modulated at a frequency corresponding to the IF, and therefore the conductivity of the bridge.

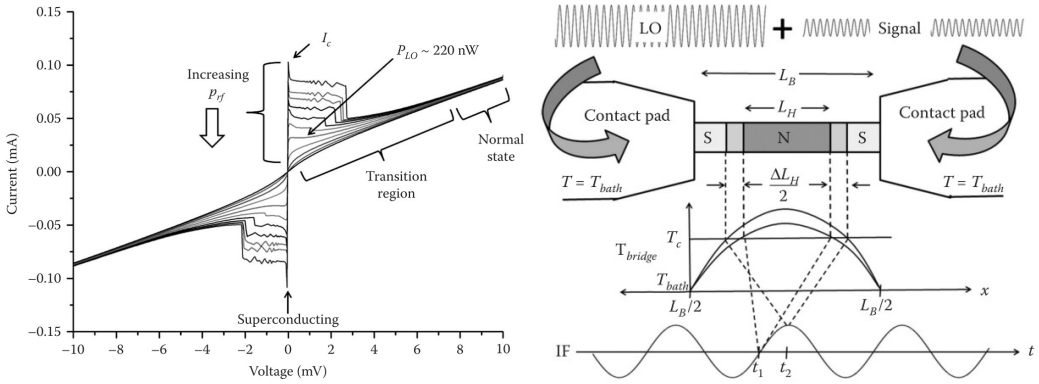

Figure 1.3: Ideal HEB IV curves for different pumping powers. b)Hot-spot model of HEB mixing. The LO and signal power are transmitted through contact pads to either end of the superconductive bridge. The bridge which is biased in order to create a hotspot where the bridge becomes normal, which size is modulated by the combination of incoming signal and LO. From [9]

The speed at which heat can be driven out of the bridge influences how high the IF bandwidth can be. The heat transfer mechanism in an HEB can happen both by electrons escaping through the contact pads, or due to electron-phonon coupling to the crystal lattice of the substrate. Depending on the distance a hot electron has to travel before losing its energy to the He bath, also called the healing distance (λ_{th}), it can be a diffusion cooled HEB[14] when $L_b < \lambda_{th}$, or a phonon-cooled HEB [17], if $L_b > \lambda_{th}$. The IF bandwidth is the quantity that determines how much of the THz spectrum can be measured (downconverted) at a given time, reaching values as high as 6 GHz, being diffusion-cooled HEB usually the ones providing higher IF bandwidths. [9, 16]

Another parameter worthy of note in heterodyne instruments is the Allan time. The Allan time is a measure of stability of the system and tells us how long we can be integrating before needing to recalibrate the system. This is a crucial parameter since the stability of an HEB receiver is a complex system due to the need for accurate biasing and optical pumping of the mixer bridge. Typical Allan times for HEB systems can go from 0.1s to around 30s depending on the stability of the system and the noise bandwidth of the measurement.[9]

1.4 Heterodyne array instruments State of the art

For practical purposes there is a necessity for having more than one single detector when carrying out astronomical observations, thus the importance of having arrays of "pixels" (parallel receivers), capable of increasing the mapping speed of the instrument and improve the data quality from measurements.

Currently only a few instruments at terahertz frequencies with limited number of pixels are functional (mainly using SIS mixers or waveguided-based HEB). There is a demand for higher frequency arrays with improved resolution and ability for multiple line spectroscopy, for example STO2 [18], upGreat [19] and the NASA candidate mission GUSTO. The main goal of this last mission is to introduce a state of the art 4x2 pixel array receiver at 4.7 THz and this thesis work aims to take a step closer. A detailed description of the mission can be found in appendix B. The main challenges in developing heterodyne arrays are the LO power multiplexing and injection, the front-end architecture (i.e.,mixers, array configuration, etc), and the circuit components integration. The available LO sources and its multiplexing are by far the main issues since it's what defines the front-end architecture of the arrays, and whose scarcity is the main reason why there are so few published results at higher frequencies.[20] In the appendix A is a summary of the operational or under development heterodyne array instruments.

1.5 Fourier Phase Grating

When trying to design an array that requires multiple mixers to be pumped at the same time, it would be non-practical in terms of complexity and tunability to use a single LO source for each of the pixels. To solve this problem researchers came up a number of solutions such as Dammann gratings or wave guide couplers[21], but the problem still lingers due to the lack of flexibility, frequency limitations, or difficulties in fabrication. The Fourier phase gratings introduced by Murphy et al(1999) and Graf et al(2001) [22, 23] is an elegant solution for this problem, allowing flexibility to the system due to a continuous phase modulation of light and easy direct milling fabrication methods. This element is crucial when dealing with multipixel QCL pumped arrays, since multi QCL implementation would be too complex to design due to this devices high thermal dissipation, requiring huge amounts of cryogenic liquids/reservoirs, and need for perfect frequency locking.

The Fourier phase grating, a reflective grating, allows user to engineer a diffraction pattern to any shape, dividing equally a single coherent incident beam into multiple sub-beams. This is possible due to the use of periodic smooth structures (cells) on its surface designed based on the Fourier series expansion theory. It uses phase manipulation of the terahertz waves in such a way that the multiple sub-beams are formed in the far field. The spatial phase modulation of a 1-D Fourier grating can be obtained by the Fourier series expansion [23]:

$$\triangle\varphi(x) = \sum_{n=1}^{N} a_n \cos\left(n\left(\frac{2\pi x}{D}\right)\right) \tag{1.1}$$

Being the unit cell defined as $\frac{-D}{2} \leq x < \frac{D}{2}$ and where a_n are the key parameters that determine

the grating surface structure. For $N = 1$ the far-field of this phase grating becomes:

$$U(\theta) = U_0 \sum_{q=-\infty}^{\infty} J_q(a)\delta\left(\theta - q\frac{\lambda}{D}\right) \tag{1.2}$$

Here $J_q(.)$ denotes the Bessel function of the first kind of order q. For $N > 1$ the modulation at the grating plane can be written as:

$$U_0 e^{j\triangle\varphi(x)} = U_0 \prod_{n=1}^{N} e^{ja_n \cos\left(n\left(\frac{2\pi x}{D}\right)\right)} \tag{1.3}$$

Which is nothing more than the product of the fields modulated by the individual fourier components, i.e, the Fourier transform of the grating. Finally, the far-field diffraction pattern of this field is obtained by the multiple convolutions of the diffraction fields of the individual Fourier components:

$$U(\theta) = U_0 \times \otimes_{n=1}^{N} \left[\sum_{q=-\infty}^{\infty} J_q(a_n)\delta\left(\theta - qn\frac{\lambda}{D}\right)\right] \tag{1.4}$$

Although equation 1.4 best define our grating, the fastest way to obtain the structure is to run a fast Fourier transform (FFT) algorithm to directly calculate the Fourier transform of the grating (equation 1.3), optimizing the a_n coefficients that best generate the desired far-field pattern (i.e, reflected beam pattern). More details on how to obtain the structure can be found in [23].

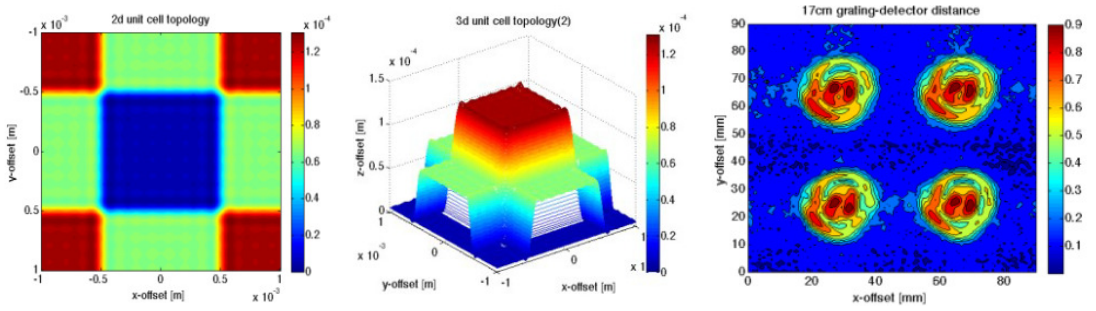

(a) (b) (c)

Figure 1.4: (a) Surface topology of one unit cell of a Fourier phase grating for 2x2 beams at 1.4THz. (b) 3D profile of the cell in (a).(c) Measurement at 17 cm from the grating. From [24, 25]

The advantages that this type of grating brings to the astronomy field is that it allows for a large number of beams to be obtained from a single source of LO, hence greatly simplifying array systems and solving the issue of the scarcity of LO sources. Furthermore, due to the dimension of THz wavelengths, this type of grating can be simply milled on a surface, without the need for highly complex lithographic systems. So far the highest frequency for which a grating was demonstrated to be an effective LO multiplexer was at 1.4THz with a 2x2 beam pattern by the works of both Y.C. Luo and X.X. Liu [24–27].

For array applications, the key parameter of the grating, besides obviously the beam pattern, is the angular distribution of the emergent beams, which depends on the unit cell size, working wavelength and order mode.

HEB characterization: 4x2 pixel array assembly

Future requirements for GUSTO will require many HEB mixers with similar performance. Part of the work here is a study of mixer performance within a fabrication batch to check the variation in sensitivity, pump power and superconducting I_c. Identified mixers are part of flight hardware selection, making the testing critical to avoid loss of devices.

It will be presented the experimental setup to characterize the HEB that will be followed by the results obtained. The setup used to characterize the HEB is the same used in the lens study in chapter 3.

2.1 HEB and Si Lens characterization setup

As explained in section 1.3, working with the HEB requires a complex setup in order to maintain the balance between key parameters such as the temperature of the bath, bias voltage, etc. The setup used in this work is summarized in the scheme found in figure 2.1a. Using our setup it is possible to bias the mixer and obtain its I-V curve, where the I_c can be extracted, and the IF output which is used to calculate the noise temperature using the Hot/Cold Y factor technique (see section 2.1.1) with the help of a hot and cold load.

The key element of our setup is the cryostat where the mixer and all the circuitry required to operate it are placed. In the cryostat we have different shields to enable the use of cryogenic temperatures: the outer vacuum shield, an intermediate shield using liquid nitrogen ($\boldsymbol{LN_2}$) at 77 K, and the inner shield, for LHe at 4 K. The last one is the most critical since is connected to the mixer block and circuitry, working as the heat sink responsible for maintaining the temperature at around 4 K, which is below the T_C of the HEB's. Connected to the cryostat we have an arm equipped with two black bodies (see figure 2.1a): one of them in direct contact with LN_2 hence working as a cold load, and the second black body, at room temperature, working as a relative hot load. A rotating mirror is used to change between loads. The well known signal is then oriented into a beamsplitter where it is combined with the LO signal coming from a far infrared (FIR) gas laser, redirecting the combination into the cryostat. The combined signal passes a heat filter which works as a low pass filter, allowing only radiation below 6 THz to pass through. After passing the heat filter the radiation is then collected by an elliptical Si lens focusing the radiation into the HEB antenna after which it is coupled into the HEB. The optical beat frequency is converted into electrical IF by the mixer. After the IF signal is extracted from the HEB, it is amplified in a cryogenic low noise amplifier (LNA). Outside the cryostat the signal is further processed by the IF warm chain, which is comprised of room temperature amplifiers, a bandpass filter, and a power detector. In appendix C the list of the instruments used for all the experiments (including grating characterization) can be found.

In figure 2.1c we have an example of the HEB chips used. All the devices characterized were produced at TUDelft. Each chip used has four spiral antennas/HEB's, referenced from A to D. Each HEB was fabricated using NbN as the superconductor material for the bridge. The width for all bridges was 2 µm and the length 0.150(A), 0.200(B), 0.200 (C), 0.250 (D) µm. The option for spiral antenna comes from the broad spectrum coverage it allows, since a single device can this way be operated between 1 and 6 THz.

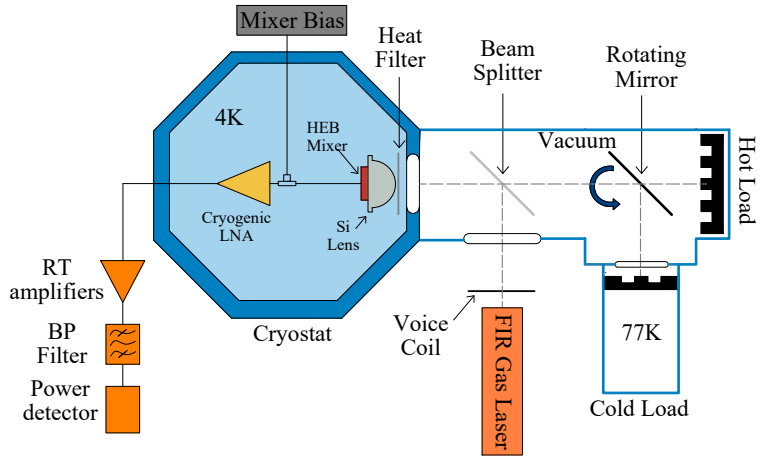

(a)

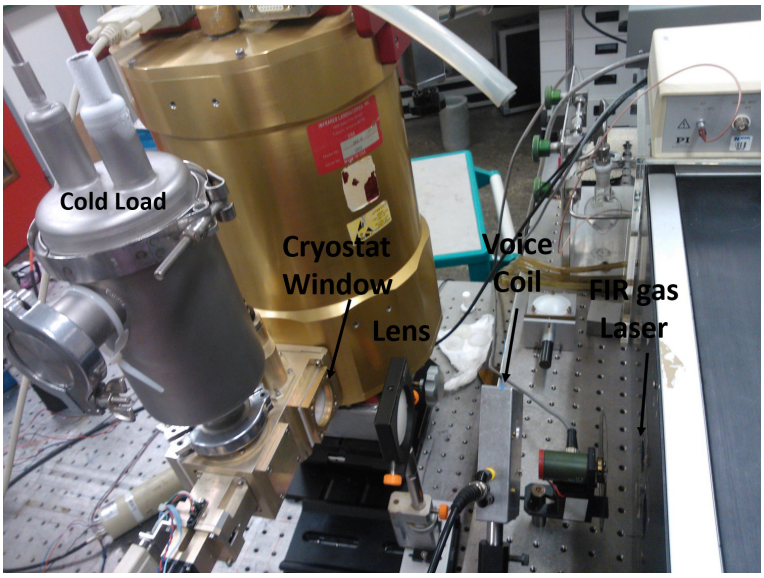

(b)

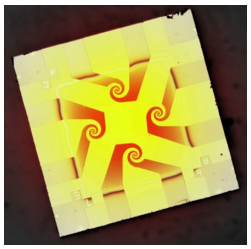

(c)

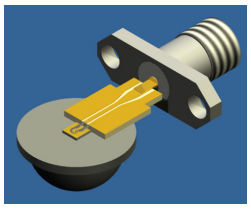

(d)

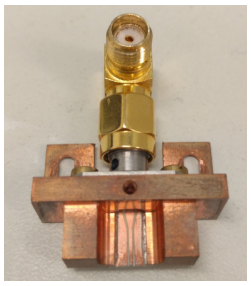

(e)

(f)

Figure 2.1: a)HEB and Si lens characterization scheme. b)Experimental setup. The lens presented can be used or not, to facilitate the radiation coupling into the cryostat. c)Example of a HEB chip used. Four spiral antenna HEB are present. d) CAD 3D scheme of the HEB mounted on the Si lens and IF/bias CPW circuitry. e) CPW circuit used. f) 10 mm lens holder used.

In figure 2.1d one can see the CAD model on how each chip is mounted on the Si lens, and how the IF/bias circuitry is connected to the HEB. For this circuitry a co-planar waveguide (CPW) is used to transmit the signals. The HEB is glued onto the lens, using a combination of an optical microscope with a micrometer XY stage to achieve alignment accuracy in the order of 1 µm. The focal point of the SI lens used is located in it's geometrical surface center at a height equal to the chip thickness. After having the chip on the lens, the mixer block is added, wire bonding the contacts of the desired HEB, with the mixer block circuit. The mixer block is then placed on the cryostat, wired to the IF chain and bias supply, followed by closing it. Vacuum levels (10^{-5} mbar) are then achieved using a two stage vacuum pump, followed by cooling,

firstly using LN_2 and later by LHe.

This setup is what we define as vacuum setup since the hot/cold signal remains in vacuum, where the best conditions for measurement are possible. Sometimes however, for greater flexibility or in the case of an array test, the vacuum setup is removed and hot/cold signal and beamsplitter are placed in air, in this case it is referred as air setup.

The FIR gas Laser works as our LO since its frequency can be easily tuned accordingly with our needs (in this work different frequencies were used, which will be addressed in the results).

2.1.1 Hot/Cold Y factor Technique

The hot/cold Y-factor technique based on the Callen & Welton noise temperature description[28] is a method that allows calculation of the noise temperature of a mixer system from its measured Y factor.

By coupling two difference noise sources (an hot and a cold load), one at a time, and measuring the output IF power of the receiver, it's possible to derive the T_n:

$$T_n = \frac{T_{hotload} - Y T_{coldload}}{Y - 1} \tag{2.1}$$

where

$$Y = \frac{P_{hotload}}{P_{coldload}} \tag{2.2}$$

$P_{hotload}$ and $P_{coldload}$ are the the output power of the receiver for each of the loads used, obtained using the Callen and Welton description of noise temperature converted to power[28]:

$$P_{CW} = \frac{h\upsilon}{e^{\left(\frac{h\upsilon}{kT}\right)} - 1} + \frac{h\upsilon}{2} \tag{2.3}$$

The T_n calculated this way will take into account all the losses in the setup due to the use of optic elements (see table 2.1), therefore it is referred as the receiver noise, DSB T_{REC}. By considering these losses it is possible to obtain the noise temperature of the HEB mixer itself as done in the work of Zhang et al [29].

Table 2.1: HEB and lens characterization setup losses.

	Type	Losses (dB)
Beam Splitter	3 µm mylar	0.2
Cryostat Window	1.2 mm UHMW-PE	1
Heat filter	QMC metal mesh W907	0.2
Si lens	Uncoated 10 mm elliptical lens	1.5
Air	20 cm, 35% humidity	0.2
Total		3.1

2.2 Results

After some preliminary studies with different devices from various fabrication batches produced by TUDelft, it was decided to study devices from a single batch, all from the same wafer defined as **NV08**. The goal here was to obtain at least 8 devices with similar properties. Only the results of this process are discussed since the preliminary tests were used with the idea of getting some experience dealing with all the process.

Although the target frequency is 4.7 THz, direct characterization at such a frequency would not be practical. With our FIR gas laser, it's not been possible to get a 4.7 THz line working, so it would require the use of a QCL, of which only one was available and there was some risk off destroying it due to improper operation (due to lack of experience of my part). Moreover it would require another cryostat, more liquid helium, which all together would take much longer to setup and would turn the experiences much more expensive. Therefore, and since for GUSTO there is also the requirement for a 1.4 and 1.9 THz array, it was decided to use the FIR gas laser tuned to 2.5 THz. This frequency was chosen because was one of the easiest to work with, with enough power to pump virtually any device (within the expected pumping power). For the characterization, only the T_n is frequency dependent, and based on previous studies is possible to extrapolate what this value its equivalent at 4.7 THz.[29]

2.2.1 In-chip device selection

When starting to study batch NV08 it was decided to begin by getting an idea of the best in chip HEB's characteristics, and then move into studying the same reference on the others chips. From the first chip, NV08_A2 we started by studying **device B**, since the bridge length is in between the other options. The results for this device can be seen in figure 2.2.

The key parameters studied were: the normal resistance (R_N), measured directly; the I-V curve, from where the I_C is extracted; the noise temperature (T_n or DSB T_{rec}); and the optimal pumping power (P_{opt}). The first thing to analyze is the umpumped I-V curve of the HEB which is measured when no LO is applied. Device NV08_A2_B can be seen in figure 2.2a, from which we can easily extract the I_C of the device.

Secondly it is needed to understand what are the noise characteristics for different bias voltages, with the final goal of finding the optimum bias conditions (i.e. where the lowest noise is measured). In order to accomplish this, different Y factor measurements are performed at several bias voltages. At each one, the following steps were taken: 1. guarantee the LO power was enough to fully pump the device (the more resistance like I-V curve the best); 2. Apply the wanted bias voltage and select the first load (Hot or Cold); with the help of an in-house Labview program, scan between two current values with a set step (usually from 20 µA to 45 µA, with steps of 1 µA), measuring the output IF power. The current variation is achieved thanks to the use of the PID control on the voice-coil, that blocks the amount of LO power reaching the HEB, inducing an increase on the current; 3. Repeat step 2 with the complementary load; 4. Using another Labview program, the minimum noise temperature is obtained based on the Y factor of the measurements in 2 and 3. For this, the data is fitted into a polynomial function , which is then used to calculate the Y factor, finally converting the Y-factor into noise temperature, where the minimum is extracted; 5. Repeat steps 2-4, until a total of 3 noise measurements were made. Figure 2.2b shows the T_n values measured this way for different voltages. The center point plotted is the average value measured, and the error bars represent the standard deviation. Knowing how the noise behaves allows us to pinpoint what the best operation voltage should be. In this case both 0.8 mV and 1 mV show the lowest values among the voltages studied, so both were measured again but using a smaller current step (0.25 µA instead of 1 µA), in order to obtain more reliable measurements. Here the T_n obtained was of 906 K at 0.8 mV and 911 K

at 1 mV. Since both were so close, 0.9 mV was also measured yielding 903 K minimum noise, at 37 µA as seen in figure 2.2c.

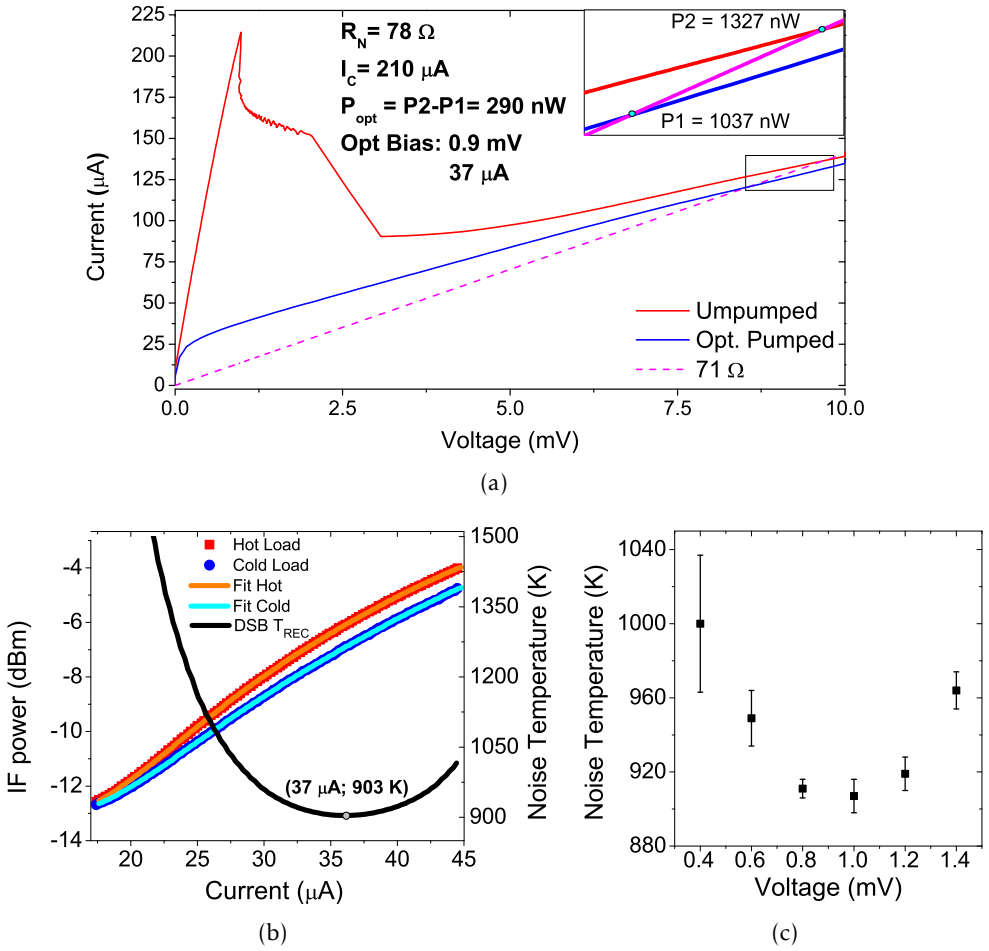

Figure 2.2: a) Device NV08_A2_B results. b) Y factor at 0.9 mV. c) Noise vs bias voltage.

For last it was measured the optimal pumping power (P_{opt}). Its calculation is based on the isothermal method [30], where a resistance line is used to interpolate both umpumped and optimum pump IV curves in the normal region. The pumping power is obtained by calculating the difference of power between both interpolation points. The optimum I-V curve is obtained by biasing the HEB with the optimum voltage, and block the LO beam in such way that the measured current is also the optimum, then a voltage sweep is performed leading to the desired I-V curve. The calculation based on this method can be seen in figure 2.2a, in this case the P_{opt} was 290 nW.

It is expected to see an increase of about 30% in the noise from 2.5 to 4.7 THz, but since the final lens will use an anti-reflective (AR) coating, reducing the total noise by about the same amount, we can assume the values measured for uncoated lens at 2.5 THz will be roughly the same as the final values at 4.7 THz with the coated lens. Therefore, the noise values for this device are within the required specifications for GUSTO, where we are looking for final sensitivities below 1500 K. The only problem is the pumping power, which is high. In order to bring down this value, **device A** of the same chip was also studied following exactly the same methods. Table 2.2.1 summarizes the data measured for both HEB A and B on chip NV08_A2.

Table 2.2: Comparison between device A and B of the same chip (NV08_A2)

Device	R_n (Ω)	I_c (μA)	$DSBT_{rec}$ (K)	P_{opt} (nW)
NV08_A2_B	77	210	903	289
NV08_A2_A	60	270	962	247

Although device A shows higher noise values, these are within the requirements for GUSTO, but the LO power required is about 15% lower, which will help in the use of the QCL + grating. It was decided to move forward studying all the A devices in the chips available.

2.2.2 HEB characterization from batch NV08

In total 10 different devices were studied. All of their data is summarized in table 2.3, the distribution of the various parameters can also be seen in figure 2.3. From those results its clearly that all devices are working and are within the specifications for noise (average 962K) and based on the average LO power required (227 nW) it will all depend on the combination QCL + grating.It should also be noted that the flatness seen in the noise temperature for device NV08_A2_B (see figure 2.2c), is present in all the devices studied, so it is possible to vary the pump power used (within an acceptable range) with little variation on the noise temperature. Furthermore, there is a clear low dispersion of values within all of the parameters, being the critical parameters standard deviation of 29 K (3%) for the noise temperature and 13 nW (6%) for the LO pumping power which might translate into a very uniform array. All of this combined indicates that more devices can be draw from this batch if such necessity arise.

NV08_A2_A due to its high I_c seems a bit off in this population. Since it was studied previously in 2013, with time the solder left from the bond wiring might have cause some effect. For this, we won't be picking this device for the array. Another HEB, NV08_B5_A, was used for all of the lens study in the following section, and although no performance issues were detected, we would rather not use it either.

Table 2.3: Summary of all the parameters obtained in the characterization of the ten devices studied from batch NV08.

Device	R_n(Ω)	I_c(μA)	DSB T_{rec}(K)	P_{opt}(nW)
NV08_A2_A	60.0	270	962	247
NV08_A3_A	64.4	185	966	216
NV08_A4_A	64.6	188	1004	224
NV08_A5_A	64.6	201	951	235
NV08_B3_A	64.4	192	968	251
NV08_B4_A	65.0	189	973	207
NV08_B5_A	66.6	181	973	232
NV08_C3_A	66.2	189	961	216
NV08_D3_A	66.2	182	884	220
NV08_D4_A	65.6	189	967	222
Average	64.8	197	962	227
Standard Deviation	1.8	25	29	13

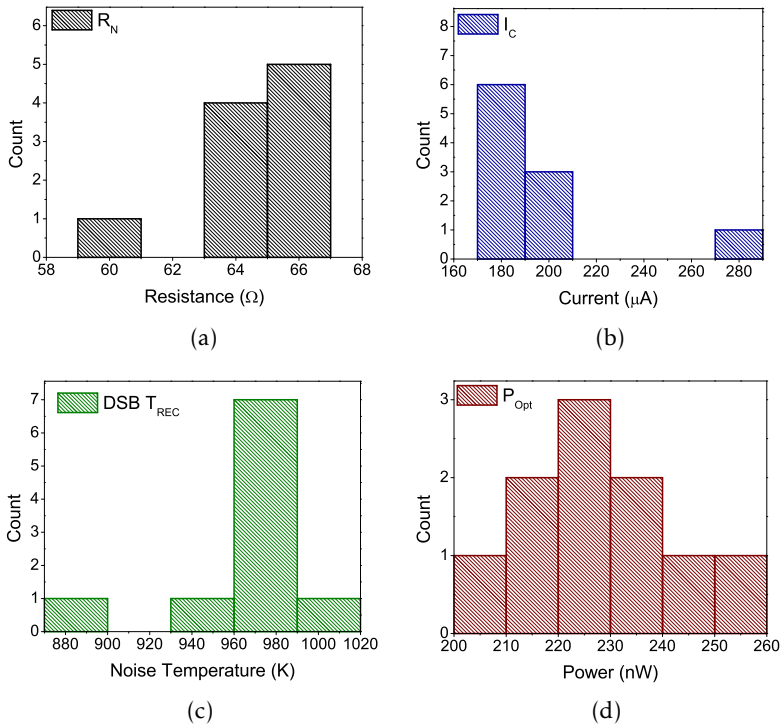

Figure 2.3: Histogram representation of the measurements. a) Normal resistance. b) Critical current. c) Noise temperature. d)Optimal pumping power.

Lens size vs noise temperature Study

One of the changes to be introduced into GUSTO from previous instruments such as STO-2, is the moving into smaller diameter lens. This will allow for more compact arrays, and therefore smaller optics systems. In order to understand how smaller lens can have an impact in the noise temperature of devices, three different lens were fabricated and then compared with the lens used in the HEB characterization, which happen to be similar to the ones used in arrays. The goal here was to discover which of the lens design was the best, and at the same time, how much noise increase should be expected. The four lens are labeled as: 10 mm (the standard test lens), L1, L2 and L3. The last three represent different designs for a 3.1 mm type lens. All the lens have an elliptical shape, following the equation $\left(\frac{x}{a}\right)^2 + \left(\frac{y}{b}\right)^2 = 1$, being the value of b and the extension length optimized assuming different dielectric constants for the lens. Table 3.1 summarizes the parameters for each lens.

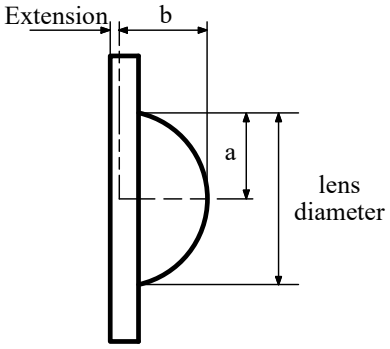

Figure 3.1: Diagram of the lens design.

Table 3.1: Parameters of fabrication for the lens used. ε_{Si} represents the dielectric value assumed for the optimization of each lens.

Lens	a (mm)	b (mm)	Extension (mm)	ε_{Si}
10 mm	5.0	5.228	1.232	11.4
L1	1.550	1.621	0.134	11.7
L2	1.550	1.623	0.141	11.4
L3	1.550	1.624	0.145	11.2

In terms of experiments, the procedure followed exactly the same steps as those used to characterize the HEB's, but this time the changing parameter was the lens, and it was used the same HEB, device NV08_B5_A.

One of the main concerns during the experiments was in guaranteeing that the thermal dissipation in the smaller lens would be the same as in the big one, since they had to be glued to the smaller mixer block used, whereas the normal one simply sits on a indium soft metal ring. Therefore, looking into the results obtained it should firstly be analyzed the I-V curves for the different lens, shown in figure 3.2. In the inset of figure 3.2a, the plot showing unpumped curves plot (see figure 3.2a) it can be seen with more detail that the curves are overlapping and that the I_C values are very close to each other. Since the bridge temperature sets the I_c, the device temperature is verified to be the same using the different lenses, hence the conclusion of the proper working and similar thermal dissipation of the device throughout the experiments. In the case of the optimum pumped curves (3.2b) it's also possible to observe the overlapping of the curves, proving the similar operation of the device and therefore allowing for direct comparison of results. There is a small difference for the umpumped curve of L3, which is due to the optimum bias conditions being different than for the rest of the lens. This change is related to the following results on the noise temperature, and the already expected bad performance of this lens.

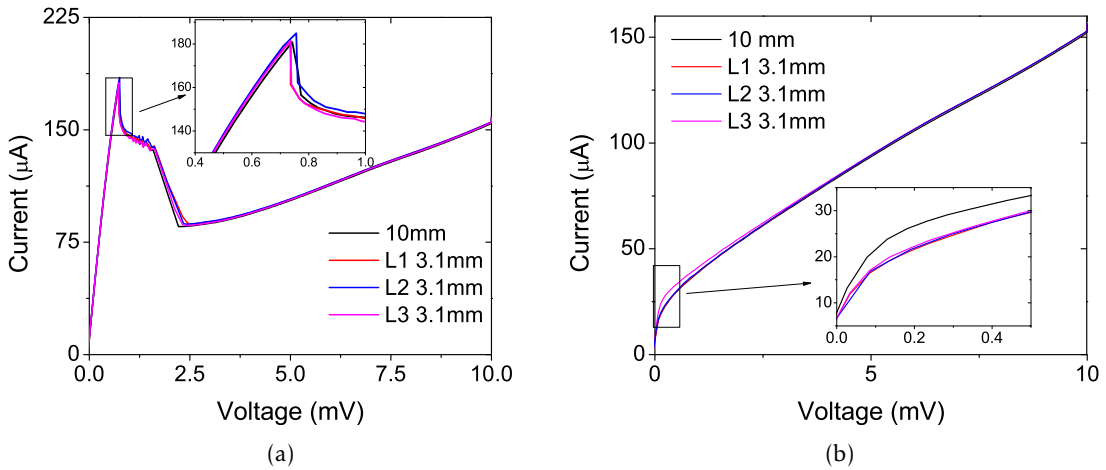

Figure 3.2: I-V curves obtained for the different lens. a) umpumped curves. b) Optimal pumped curves.

In figure 3.3 the Y factor measurements for each lens at the best bias conditions are plotted, while table 3.2 summarizes the minimum for each of the measurements and it's bias conditions. Early experiments on the noise measurements lead to the use of a 15 µm beamsplitter to pump L1, later solved by using a lens to focus the LO power into the cryostat (used in the experiments of L2 and L3). This lead to no real data being available for the 3 µm beamsplitter for L1. Based on the measurements for the 10 mm lens and L2 where both beamsplitter have been used, it was possible to make the beamsplitter correction from 15 to 3 µm thickness and obtain the curve for L1.

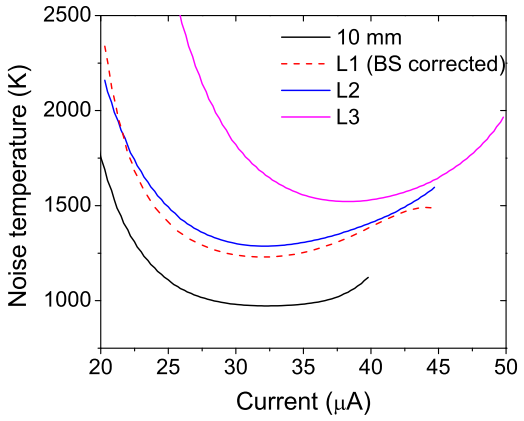

Figure 3.3: DSB T_{rec} for device NV08_B5_A using different lens. Data for 3 µm thickness beamsplitter.

Table 3.2: Minimum noise and optimum bias conditions for the curves in figure 3.3

Lens	V (mV)	I (µA)	T_n (K)
10 mm	0.6	32	973
L1	0.6	32	1230
L2	0.6	32	1287
L3	0.6	38	1522

Based on the results obtained is clear that there is a similarity between L1 and L2, with L3 being very different, even in the optimum bias conditions. The bad performance for L3 was already expected since the dielectric value for which it was optimized (11.2) was known to be wrong. The main conclusion here, besides that the design of L1 seems to be the best, is also the increase of approximately 26% in noise between the 10 mm diameter lens and L1, which still sits within the desired noise requirement for GUSTO.

In an attempt to better understand the results obtained, the lens performance was simulated based on the real dimensions measured. This was performed by Ricardo Farinha at TU Delft and more details can be found in his work [31]. Table 3.3 summarizes his measurements results and

comparison with the optimum values obtained through simulations. The simulations assumed the correct ε_{Si} at cryogenic temperatures to be 11.4 . Some differences between the measured parameters and the original design that can highly impact the real efficiency of the lens. This is clear in figure 3.4 where the lens efficiency vs extension length for all the lens are plotted. These results indicate that L1 and L2 should have similar efficiency and therefore similar noise behavior, which confirms the experimental results. The difference is that L2 was expected to be the best which is not the case. Since the values obtained via experimental work are very similar, the cause for this difference could be due to noise in the measurements, or a small HEB misalignment from one measurement to another. A important conclusion that can be drawn is that any small variation on the extension length or the substrate (chip) thickness can have a very high impact on the device performance. This can also be applied to misalignment of HEB when placing them on the lens.

Table 3.3: Extension length without the substrate thickness for the optical measurement. It also shows the distance from optimum extension, simulated in PILRAP

Lens	Expected extension (mm)	Optical measure (mm)	Variation (µm)	Δ optimum extension (µm)
10 mm	1.229	1.232	+3	+27
3.1 mm lens 1	0.134	0.152	+18	+23
3.1 mm lens 2	0.141	0.148	+7	+22
3.1 mm lens 3	0.145	0.156	+11	+32

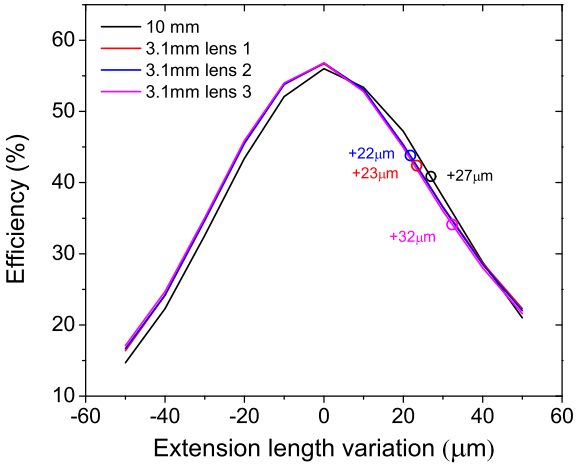

Figure 3.4: Simulated curves of the lens efficiency vs the extension length.

During the experiments a feeling of uncertainty towards our vacuum setup started to build up. The reason for this is that in the vacuum setup, the hot/cold load has a limited size, and since the lens diameter changes there was a chance of this limitation to affect the measurements, e.g. the misalignment between the loads and lens position inducing error. In the air setup (figure 3.5), the loads are much bigger, which allow to fully cover the cryostat window, hence making sure that any lens within its diameter to receive the maximum radiation possible from both loads. Therefore, to complete the lens characterization it was decided to study the impact of the air vs vacuum setup on the noise measurements.

The results obtained for air vs vacuum setup are plotted in figure 3.6. The first detail that should be noticed is the I-V curve difference between the sets of data for air and vacuum measurements. There is a decrease on the I_C from the original 181 to 171 µA. This drop is caused by the larger diameter of the optical components used in this setup, which causes more radiation to be introduced into the cryostat, heating the mixer block and therefore the device, hence this change. In terms of noise measurements there is an interesting difference on the increase of noise for both lens: in the case of the 10 mm lens the noise increases about 28%, while for L1 the increase is only 17%. It was expected that the change be the same in terms of proportion, and since we have such a difference we conclude that our hypothesis was right. On one hand both lenses suffer from the same issues from vacuum to air: we have loss of the load signal by absorption when passing through the cryostat window, plus the absorption in the optical path by the air humidity (which is expected to be much smaller than the previous noise source, although difficult to quantify), these effects cause for the signal-to-noise to be reduced. At the same time the loads source are much bigger, so basically it is possible to be sure that no misalignment exists between the lens and the sources, which in the case of the smaller lens, allows it to see all the radiation from the cold load (possibly our problem), and this way, improving the noise temperature which compensates for the negative effects, thus the variation detected being smaller for L1.

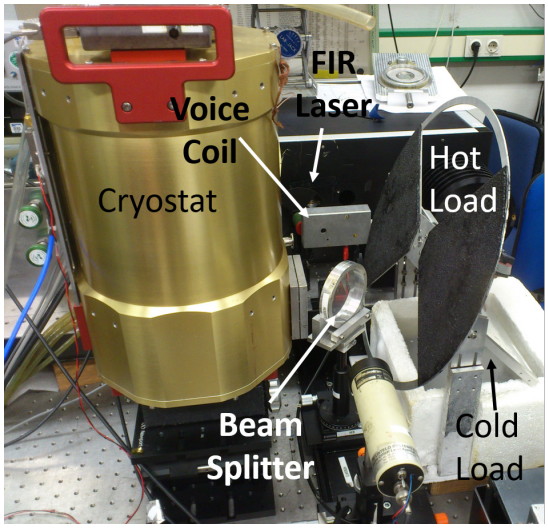

Figure 3.5: Air setup

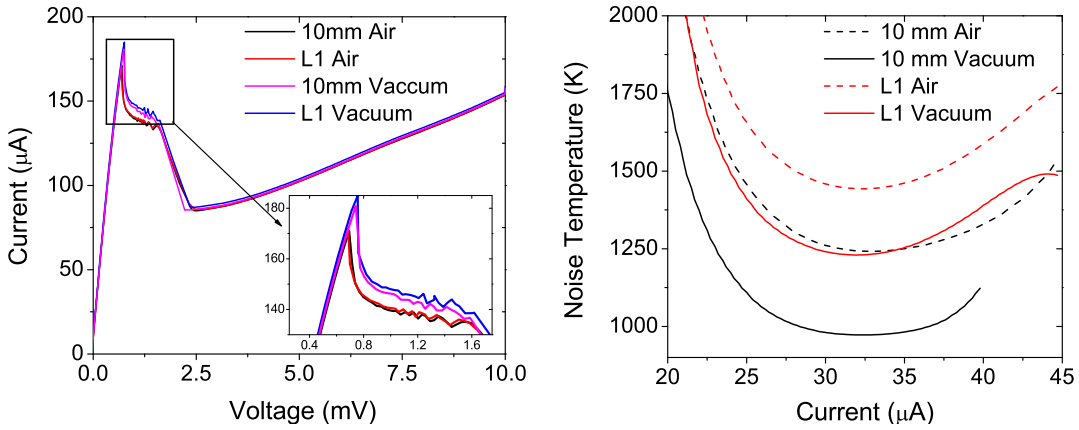

(a) (b)

Figure 3.6: Air vs Vaccum setup results. a)I-V curves. b) Noise curves at the optimum voltage. The minimums are: 1443 K - L1 Air; 1242 K - 10 mm Vacuum; 1230 K - L1 Vacuum; 973 K - 10 mm Air.

Although more experiments are required using improvements to the vacuum setup, it can be concluded that although the noise temperature increases with a smaller lens, it should be anticipated that the increase under vacuum conditions will be below 26%, from the best value

obtained for L1 and concluded to be an overestimation of the real noise. Even assuming this value as the real one, it would set the average noise temperature of the receivers characterized in the previous chapter around 1200 K which is still below the GUSTO requirements, allowing the conclusion that it is possible to move into smaller lens in the future arrays.

Fourier phase grating characterization

The characterization of the Fourier phase grating represents the core work of this thesis and as a result presented the greatest challenge. The Fourier grating works, effectively, as a splitting mirror with angular offset for each of the 8 intended beams. To properly understand its behavior, the beam pattern reflected off of it with a collimated incident beam was studied, from where it is possible to extract the angular distribution and efficiency, the key parameters for the real application of the grating.

Previous works on gratings [25, 26], already showed promising results for 2x2 pixel arrays at 1.4 THz. For GUSTO the goal is to get a 4x2 HEB mixer array pumped using this method of LO division. For this, a new grating designed to produce a 4x2 beam pattern at 1.4 THz was fabricated. This frequency was chosen due to test setup limitations which do not provide an opportunity to study at 4.7 THz. A benefit of initial testing at the lower frequency is to make use of previously gatherer knowledge from past works at the same frequency. This particular grating was designed by B. Mirzaei (PHD student at TU Delft) and was fabricated at Arizona State University (ASU). The designed maximum groove depth is 93 µm, maximum curvature radius of 106 µm and unit cell size of 2 mm x 2 mm. The simulation of the surface profile, the profile of the final fabricated grating and the grating comparison between designed and real surface are shown in figure 4.1. The surface fabricated was also measured by B. Mirzaei, where it was noticed some differences (marked with a red area in figure 4.1c).

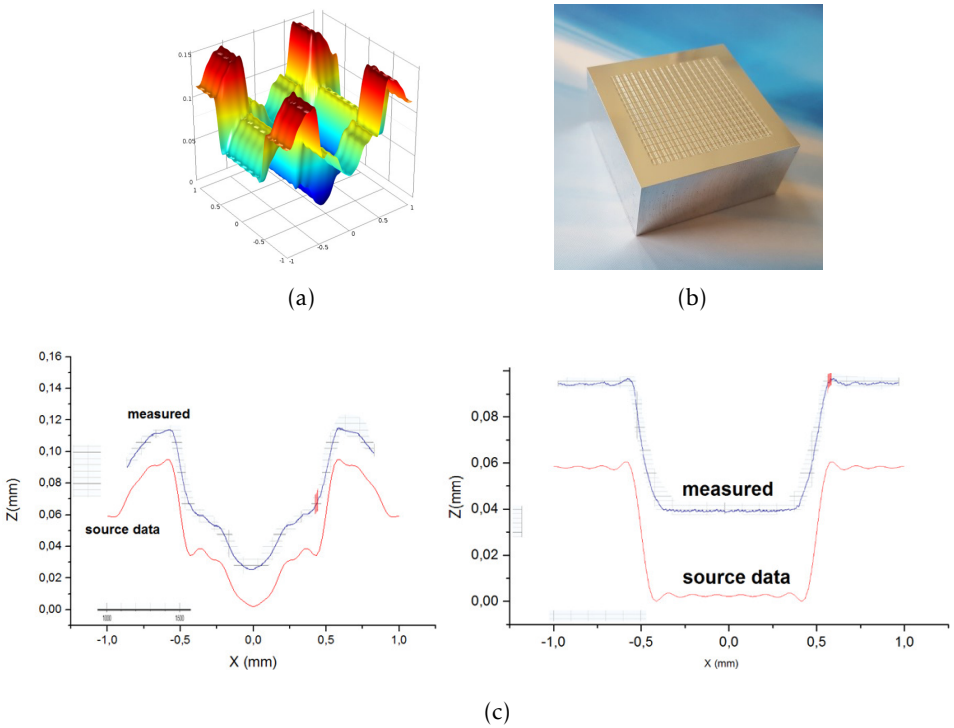

Figure 4.1: Fourier phase grating. a)Simulation of one unit cell. b) Fabricated grating (machined surface: 3 cm x 3 cm). c) Profile comparison between measured (real) and source (designed) data. Note: Z offset added to improve visualization of the results, it's not a real difference.

4.1 Experimental Setup

The grating beam pattern was characterized using the scheme presented in figure 4.2.

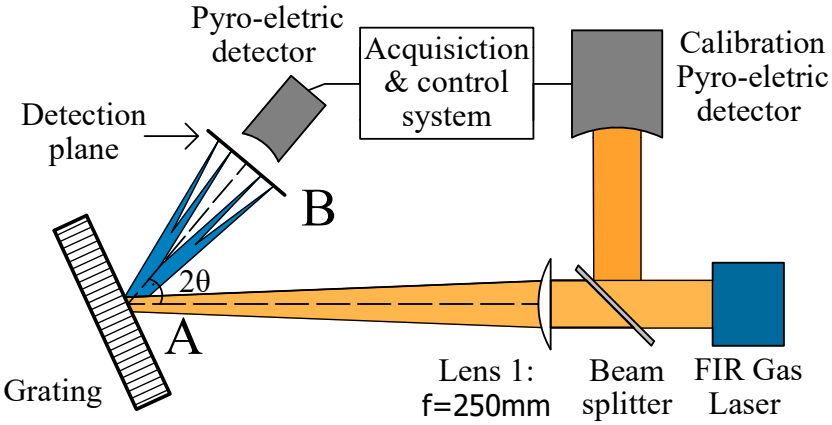

Figure 4.2: Scheme of the experimental setup for the Fourier Phase Grating characterization.

The FIR gas laser is tunned to emmit a 1.4 THz collimated laser beam. This beam passes through a beamsplitter which reflects 5% into a pyro-electric detector used for power reference measurements, since the laser output power is not stable. The laser beam shape is not uniform, but since the laser power is proportional to signal, it was decided to use of a focusing lens to maximize the THz beam. This lens, made of high density poly ethylene (HDPE), typical material for THz lens, has a high focal length (250mm) and the optical path is adjusted for the focal position to coincide with the scan plane, which is at 60 mm from the grating. This way it would be possible to resolve small beams, and therefore the shape of the beam pattern, while at the same time allowing the grating to be illuminated by a large area beam, crucial for its operation. The grating is positioned in the optical path of the beam with an angle θ with its normal, causing the reflection of the multi-beams with a 2θ angle in relation to the original beam. At the desired distance from the grating (measured from the center where the beam hits the grating) the beam pattern is measured using another pyro-eletric detector. This is possible combining the detector with a XYZ raster scan. The raster scan is controlled by a control and acquisition Labview coded routine, which besides controlling the raster scan, also collects and plots the values measured by both of the detectors into two different matrices. The values measured on the calibration detector are used to normalize the data on the beam pattern measurement (this process is described with detail in section 4.1.1). The purpose of the reference is also to pause the scan should the THz emission of the FIR laser fail during these long period scans.

As previously described, the incident gas laser LO beam was carefully measured since is necessary for the efficiency calculations, but it is also crucial to understand how the grating might transform the beams. Figure 4.3a shows the beam incident on the grating, and in figure 4.3c the shape of the single beam at the same position as the beam pattern measurements, represents A and B respectively on figure 4.2. The first figure clearly shows that although the beam is small, it still covers many unit cells. This is the beam used as the reference for the efficiency calculations. The later beam gives out the expected shape of each beam at the

scanning plane. It should be noted that this images are obtained through some data treatment which will be detailed later in this chapter.

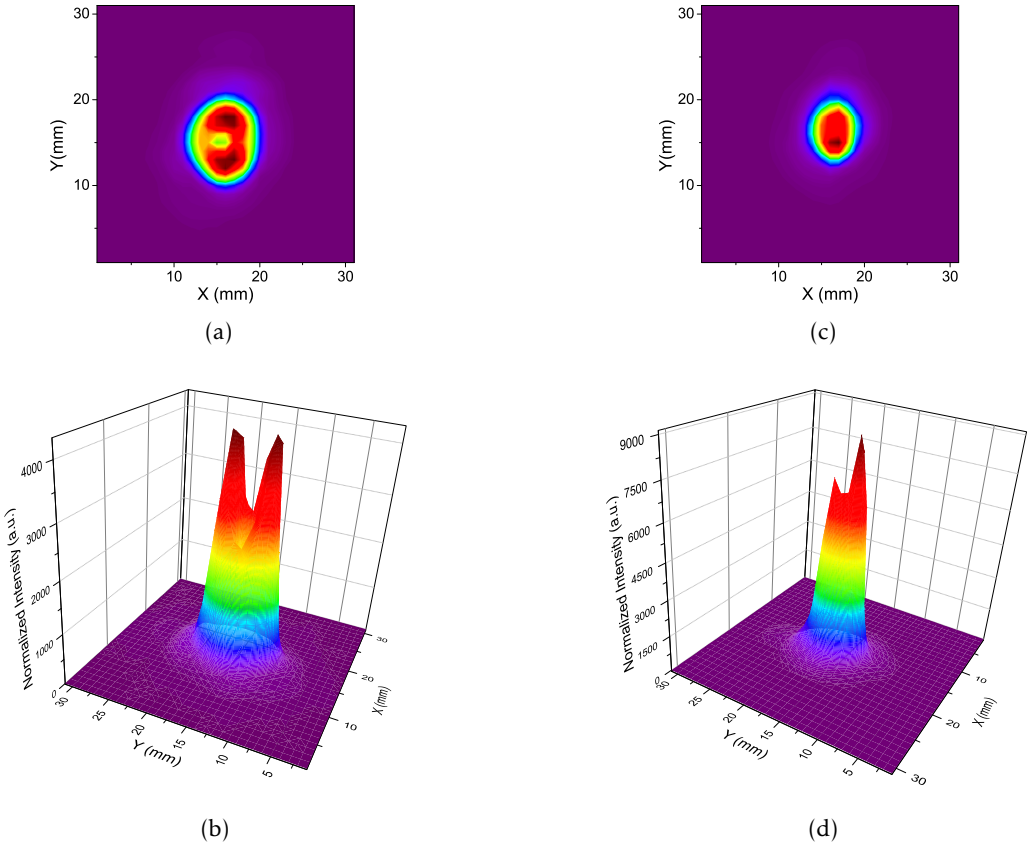

Figure 4.3: Incident LO beam. a) and b) Beam measured at the grating position (Lens + 190 mm), 2D and 3D representations. Represents point A in the experimental setup. c) and d) Beam measured at the equivalent scanning position (Lens + 250 mm), 2D and 3D representations. Represents point B in the experimental setup for the single beam.

The importance of using the focusing lens can be understood by looking at the beam pattern of the beam incident on the grating. In figure 4.3b it's clear its non uniformity of the original beam. When we compare this beam with the one obtained after 60 mm (figure 4.3c) we can see the one of the peaks almost disappeared. This happen since it was tried to focus mainly the highest intensity beam, otherwise there would always exist a double peak system which would make it harder to use it to study properly the grating. Also, it can be seen that the beam, although smaller, is not as concentrated as it was expected so close to the focal point (it's impossible to be sure that the scan is precisely positioned at the focal point). This leads to the conclusion that the emitted beam from the FIR gas laser is not totally collimated.

4.1.1 Data acquisition and treatment

The characterization of the grating was performed at different angles θ: 15º, 20º and 25º; at a fixed distance of 60 mm from the grating. The raw data obtained was measured with 1 mm scan step size, which defines our spatial resolution.

When measuring the beam pattern it was found that the laser would drift randomly between different values through time. Therefore it was decided to use a pyro-electric detector to act as

reference. The first step however was to check if there was a linear relationship between the laser power being measured in both detectors. This was achieved by placing the main detector at the peak of intensity of the beam, after the focusing lens. Main beam and reference beam power levels were then recorded simultaneously to check for linearity. The change in beam power was achieved by introducing materials with different attenuations (e.g. beamsplitter with different thickness) at the FIR gas laser output. The data is plotted in figure 4.1.1 along with the linear fit. It is clear the linear relationship between both, which proves that we can use the data from the reference to normalize the measured data.

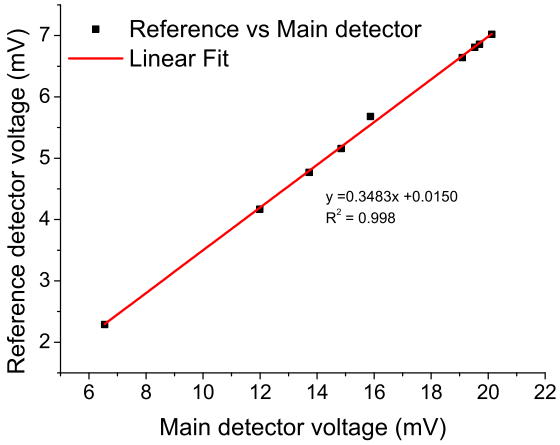

Figure 4.4: a) Calibration curve of the data

Looking at an example of the raw data obtained from both measured data and laser reference it can be understand how crucial this correction is. Around the middle of the experiment there was a drop on the laser value of about 15% (see figure 4.5b which induced the pattern being measured to appear to be weaker on the right part of the measured pattern (figure 4.5a. Since we know that the reference and the data measured always have a linear relationship, the correction of any change in laser intensity is achieved by simply dividing each data point measured by the equivalent value measured on the reference pyro-electric detector.

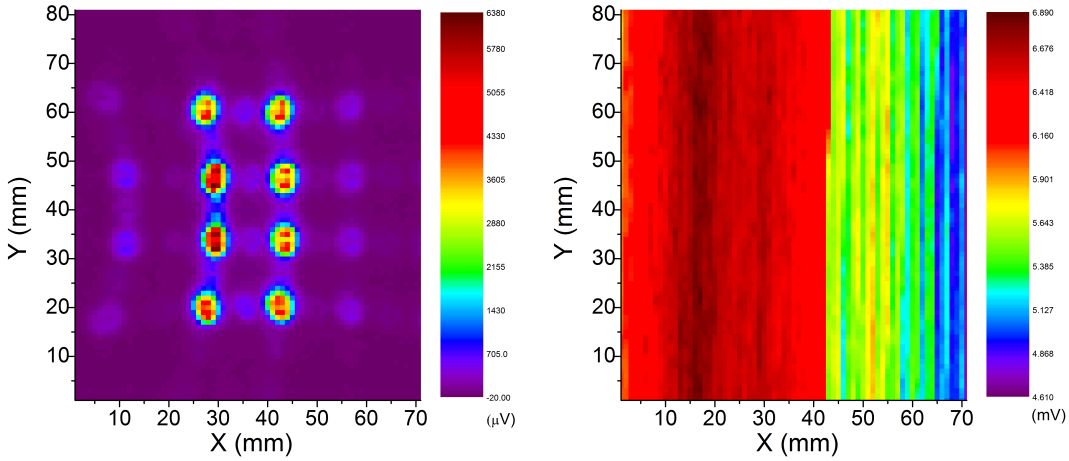

(a) (b)

Figure 4.5: a) Raw data measured at 25º. b)Correspondent laser values measured as reference.

The corrected image is shown in figure 4.6a. There it can be seen changes to the right part of the image, which now accurately represents the pattern. Due to the small beam size and the spatial resolution used, the beam shape is under sampled, inducing the direct imaging of the data to be less clear than desired. Therefore, the graphing and data processing software Origin was used to improve the quality of the image. The software allows the user to interpolate the data points and plot the result as contour plot (excluding the contour lines) which smooths out the image. Another option could have been the use of increased resolution (e.g. 0.5 mm steps) but for every halving of the step size, it would take four times longer to achieve the same scan. Since our detector area is enough to cover the step used, the power resolution will be the same, tests of resolution vs integration values yield differences smaller than 1%, thus indicating that no gain would be achieved with higher spatial resolution. Figures 4.6a and 4.7d show the direct imaging and the Origin processed version of the normalized data. All the results are shown in linear scale as this better represents beam positions and shape.

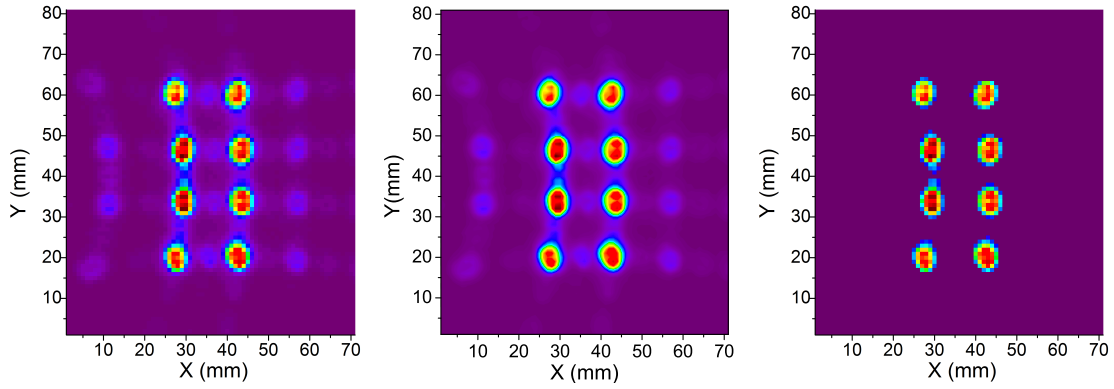

(a) (b) (c)

Figure 4.6: Beam pattern at 60 mm from the grating at 25 Degrees. a) Direct Imaging. b) Origin contour plot. c) Direct image after noise removing algorithm.

For the efficiency calculations it was compared the total power measured from the incident beam on the grating (figure 4.3a) with the total power of the eight beams generated. Since the beam pattern includes noise and other artifacts caused by the grating surface (discussed later), the main beams were isolated from the noise background using a threshold method. To obtain the threshold value the normalized data was plotted directly, and by changing the minimum data level displayed, it was possible to interactively obtain the threshold that both removes all the noise, but at the same time keeps the beam shape intact. A Matlab script was then written to set to zero all the normalized data values below the discovered threshold. A representation of the data after running this noise removal method can be seen in figure 4.6c. Finally the efficiency is calculated by integrating and comparing the data from both the result of the noise removing method and the normalized single beam. The integration is obtained by summing all the points. Since the data from the beam patterns was obtained used a 1 mV scale, and the single beam, a 10 mV scale, there is a different noise floor. Combining this with the smaller area scanned for the smaller beam, it was realized that using a threshold method would induce additional error. Therefore, for the single beam, only normalized data was used without applying further noise corrections.

4.2 Beam pattern results

Analyzing the results obtained at each incident angle, θ, are summarized in figure 4.7, one can see how similar the shape of each generated beams is when compared to the expected beam shape (single beam, see figure 4.3c), the expected mirror like behavior. Looking to the overall pattern it is clear that as the angle of incidence increases the beam pattern deteriorates. At an angle of 15º is where we see the best uniformity in the distribution, although it's already noticeable that the lower left beam is smaller and slightly more misaligned relative to the beams in the same column. This last effect can also be seen for the top left beam. At 20º some tails start appearing at the left central beams, increasing the effect at 25º where other beams also evidently present this behavior. Moreover, it's clear that the peak intensity of the beams at the edges are getting less powerful as we move into higher angles. This doesn't necessarily means that the beam in itself has less total power, simply that the beam can be bigger in area and the total integration power could be actually similar. This hypothesis was tested for the pattern at 25º by isolating each of the beams by area and integrating them separately. It was calculated that a 29% difference in total power between the more powerful beam, which is the top left in the central four beams, to the least powerful, the top left one(outer beam), therefore refuting the hypothesis. This was obtained by calculating the power of each beam separately after the noise correction. In terms of geometric shape the most suitable for real applications is seen at 15º, where the relative power beam distribution is the following: the strongest beam is the lower right, followed by the top right with about 89% relative power. The weakest ones are the center top left and top left beams, both with approximately 79% relative power. The rest are all within the same values, averaging 87% relative power.

On these images it is also possible to see some higher refraction orders (the aforementioned artifacts). They are present close to the edge of the images, where it can be seen some faint darkblue features. These beams are basically unwanted copies of the incoming beam at different locations other than the wanted pattern. These refractions are minimized when the design is generated, but since there are changes on the manufactured grating, due to limitations in the fabrication, they can become more relevant. These elements are the main cause of efficiency loss in this type of gratings and explain why the maximum theoretical efficiency is always somewhat lower than 100

These results agree well with the simulations obtained at the same distance and presented in figure 4.8. It should be noted that these simulations are based on the designed and not real surface and assume a perfectly collimated gaussian beam. Here we can see the same behavior as in the measured results, where the least skewed pattern is the one obtained at 15º and that as we move into higher incident angles we got increased curvature, and less intensity on the outer peaks. This simulation results only show the main beam pattern part in order to save computing power, since the simulations required can take some hours to run.

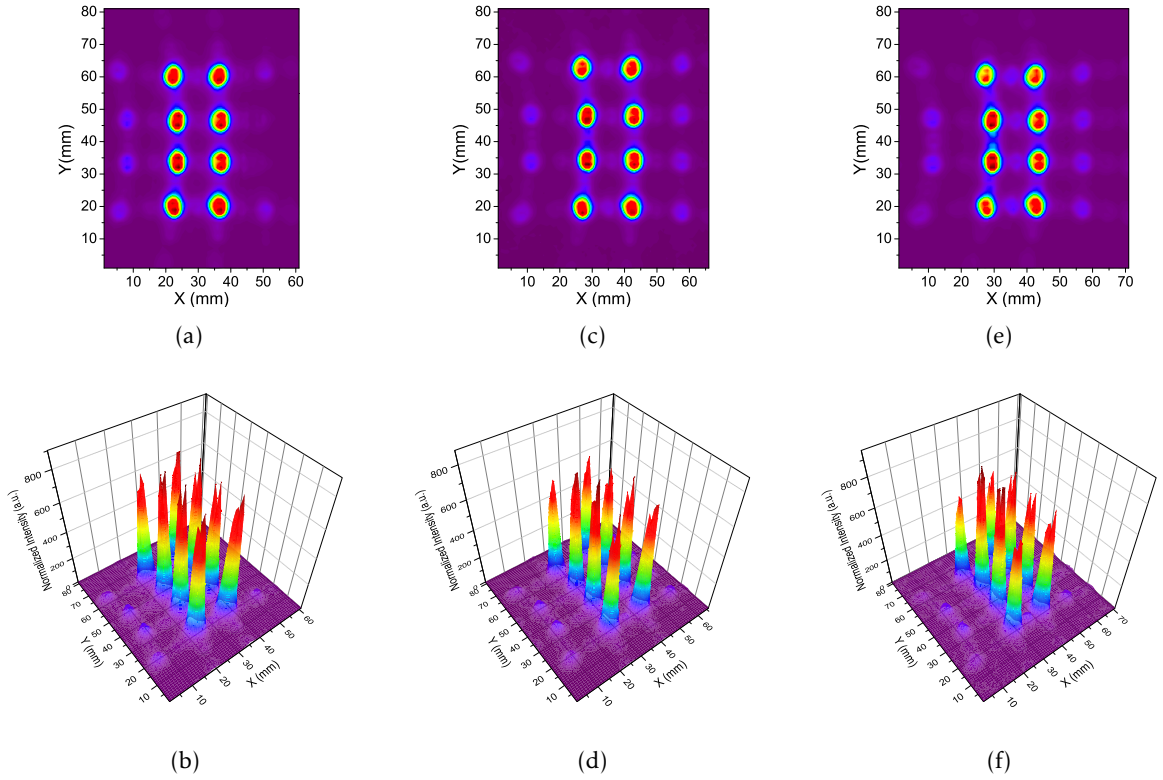

Figure 4.7: Beam pattern results. Top and bottom images show the 2D and 3D representations respectively. a) and b) 15º. c) and d)20º. e) and f) 25º.

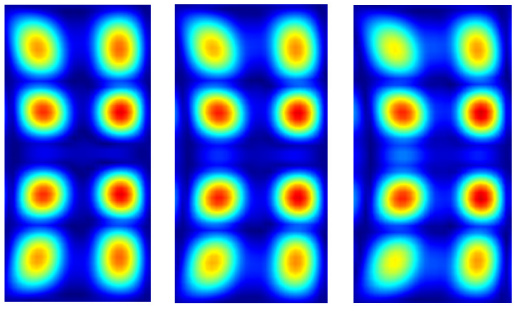

(a) 15º (b) 20º (c) 25º

Figure 4.8: Simulated beam pattern based on the designed surface and perfect collimated gaussian beam. a) 15º. b) 20º. c) 25º.

The values obtained for the efficiency are reported in table 4.1. The main conclusion that can be draw is that both 15º and 25º have almost the same efficiency, so in terms of application the geometric shape of the pattern is the decisive factor, which is clear to be the best at 15º. Comparing the efficiencies of the simulated and measured results, the main issue is the high discrepancy at 15º, where we have a difference of 25% efficiency. Looking into the beam patterns and single beam power integration it was obtained a maximum difference of around 20% relative power, while from the simulations it was expected that the relative power of the outer beams to revolve around 50%. The reason for this might lie within the mismatch between the designed and real surface as shown in 4.1c. Actually this is an interesting result in the sense that the grating in reality has a much more uniform beam pattern than expected, thus more

easily applicable on an array.

Table 4.1: Efficiency values for both simulated and measured results.

	15º	**20º**	**25º**
Simulated (%)	45	53	58
Measured (%)	71	64	69

It should also be noted the error underlying the real data measurements, which can be affecting the results. After a lot of discussion on this topic it was concluded to be difficult to quantify exactly the error values for the efficiency. First we are normalizing each of the measurements with the data from different detectors, so in the end the final data, although improved, might have some mixed noise floor. Besides this, another and probably bigger source of error could be the threshold method. Using this method it was seen variations of efficiency ranging 3-5% due to changes on the threshold of about 20%, but even this error is minimized by not applying the noise removing algorithm to the single beam used as reference, thus being conservative results. So, although we are quite confident on the values obtained, it is quite difficult to accurately assess the error bars for this particular set of results.

The scanning plane pays an important role on the perception of how the grating behaves. It was chosen a 2D scanning plane since it matches one of the most used and simple geometrical architectures for arrays focal planes. The issue with this plane is due to the existence of different angular offsets for the outcoming beams it causes scanning two-dimensions planes to scan beams with different traveling distances (distance measured from the grating to the scanning plane, see figure 4.9). This is the main reason why it is also seen some curvature to the left on the beam pattern shape, although the accuracy available to position the detector can also have some impact on this, being difficult to have exactly the same θ between the normal of the scanning plane and the normal of the grating, as there is between the normal of the grating and the incoming beam. The only way to solve this issue would be to measure in a spherical surface, which was only realized later on the characterization work, and although possible to achieve using the raster scan, would be way too complex endeavor for the limited thesis time available at that point. One problem of using a spherical surface would be it's representation on a 2D surface, since it's impossible to do it without a certain degree of distortion (which would depend on the type of representation, similarly like what happens with 2D representations of the Earth globe).

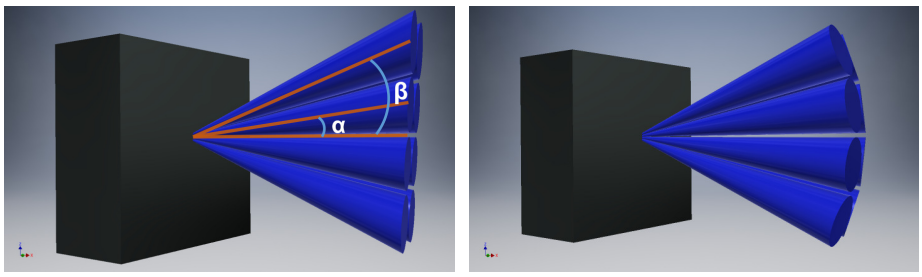

(a) (b)

Figure 4.9: 3D simulation of the grating beam pattern. a) Flat plan intersection. Representation of the side angles. b) Spherical plane intersection.

Based from the best beam pattern (15º) the angles can be calculated using the following relationships : $\alpha = \arctan(s1/d)$ and $\beta = \arctan(s2/d)$. The distance, d, is known to be 60 mm. a1 and a2 are the distance from the center of the image to the center of the closest and farthest beam respectively, in the same column. From the images it can be extracted that $s1 = 6mm$ and $s2 = 19.5mm$ (based on our resolution). The angles are approximately $\alpha = 5.7º$ and $\beta = 18º$.

All work until this point has dealt with a grating mounted in a vertical plane so that the pattern measures 4x2 in the Y and X axis respectively. In terms of applications of the grating it can be interesting to use it's beam pattern rotated by 90 degrees, having 2x4 (2 rows of 4 beams) instead of the 4x2. In order to study this, the grating was rotated and measured again at 15º and 25º which beam pattern are reported in figure 4.10. Due to the angular distribution of the beams, it was already expected that some issues would arise from the rotated grating, which can be clearly seen at 15 degrees. There, the right two beams are much weaker than the rest. This happens because these beams are the ones closer to the original path of the incident LO beam, and when the detector used is scanning this zone, it blocks partially the incident beam. At 25º the two left beams, far away from the original beam path also are shown to be much weaker than the rest. This was already expected from the simulations (see figure 4.10e, being probably caused by how light interacts with the grating. Since the unit cell is not symmetric in x and y direction, by changing the structure the light illuminates, there is a change in the final beam pattern, which is further amplified as we move into higher angles, since it is moving away from its designed angle. Based on this experiments it is concluded that the beam pattern using the grating rotated is not viable for the desired application.

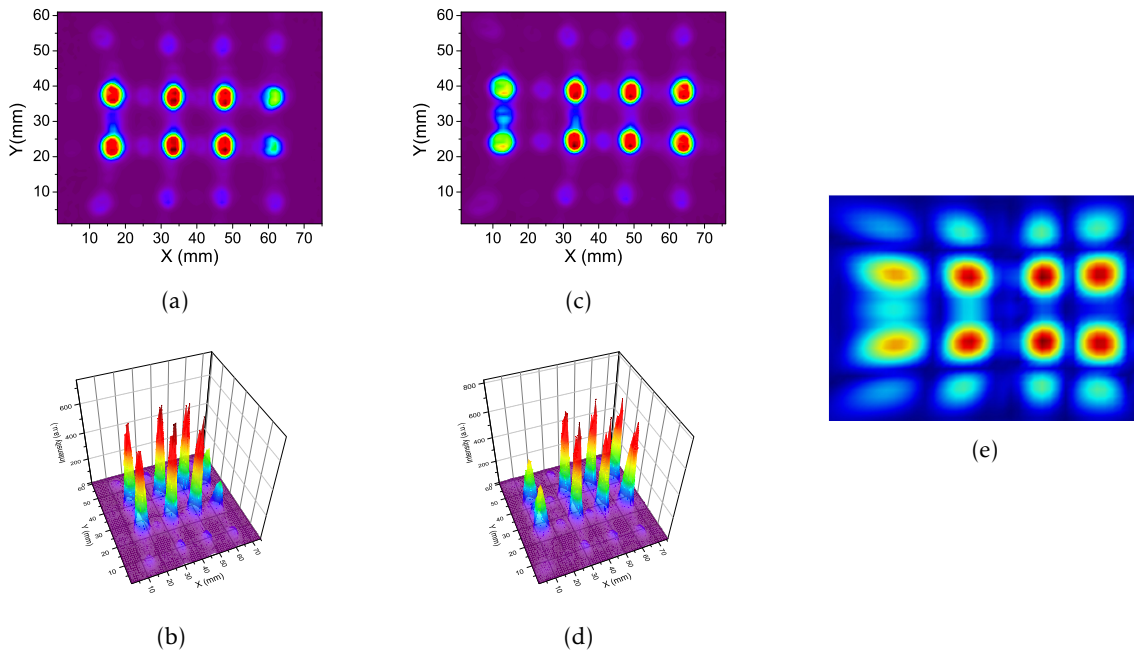

Figure 4.10: Beam pattern of the rotated grating at 60 mm from the surface. a) and b) 15º. 2D and 3D representations. c) and d) 25º.2D and 3D representations. e) Rotated grating simulated at 25º.

4.3 Array demonstration

Having characterized the grating at 1.4 THz, the next step was to apply it to an HEB receiver array and attempt to sufficiently pump multiple mixers. The previous work in our lab already had in place an 2×2 pixel array with a distance between the center of the beams (pitch size) of 11 mm, which was used to study the previous 2x2 grating at 1.4THz. Due to time constrains it was decided to use this array as a sort of sub-pixel array, which would be used at different Z off-sets to simulate a full 4x2 array. All the details for this array can be found in [26]. It should be noted that due to the fragile nature of the IF CPW circuitry of the array block, two of the pixel circuitry was damaged, leading to some series resistance to be added. Nevertheless, it was still possible to use them as functional pixels since all it is required is for two clear states to be seen, pumped and umpumped.

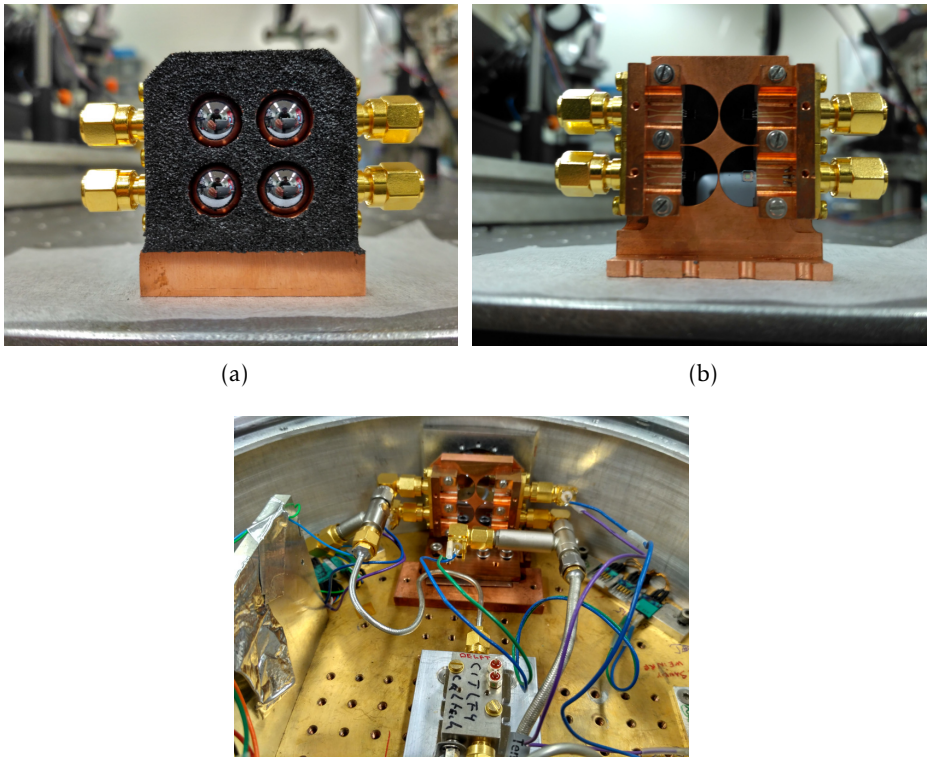

(a) (b)

(c)

Figure 4.11: 2x2 HEB mixer array block. a) Front view. b)Back view. Its possible to see the small HEB chips glued in the center of the lens. c) Array block mounted on the cryostat and connected.

4.3.1 Optical Path design

Applying the grating as an effective multi-pixel pumping system is not as simple as characterizing it. To start with, the beams coming out of the grating are not parallel, therefore, it would require the position of the cryostat at the exact perfect distance from the grating surface, in order to match the beam pattern to the array dimensions. This in turn would be impossible without blocking the incoming laser, due to the dimensions of the cryostat. Therefore it is required the use of a lens to collimate the pattern. Since the beam pattern has to match the array design, it must be taken into account the pitch size of the beams and the spot size of each beam, which shouldn't be bigger than the lens used, i.e. 10 mm diameter, in order to make use

of the entire power.

Although looking like a complex system to work with, a single lens positioned in front of the grating could solve all of these constraints at once. Firstly, assuming the divergence of the pattern of beams starts at the grating, by placing a lens at such a distance from the origin of the beams that it matches its own focal length, would achieve the collimation of the pattern. Moreover, a well designed lens would have an focal length that would allow for its position to gather the beams with the desired pitch size, while the the small size of the beams was already obtained with the focusing lens used in the characterization.

It was first attempted to collimate the pattern of the center four beams (in figure 4.12a these beams are highlighted). The selection of these beams is logical, since it would be the easiest way to match the grating output to the existing array. Based on our calculations, using the angle α measured, the ideal lens should have a focal length around 55 mm. Since in our laboratory the closest available was one with 50 mm it was used instead. After initial attempts it was realized that having a double lens system (the first to focus the incoming beam and the second to collimate the beam pattern) plus the optical effect of the grating, created an overly complex system to work with due to the different focus length of both lens (250 mm vs 50 mm). It was quickly decided to adopt a different approach: swap the first lens with an aperture stop.

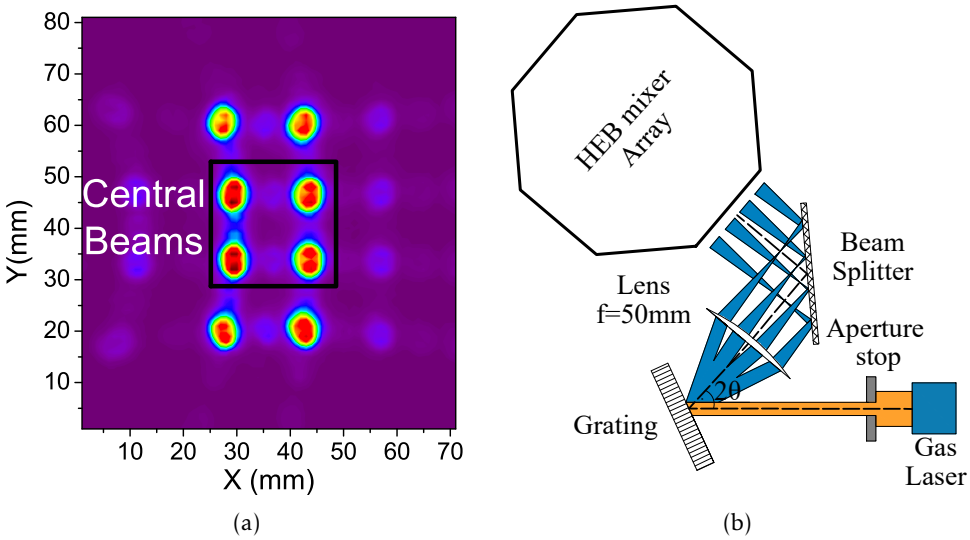

(a) (b)

Figure 4.12: a) Highlight of the central beams for the pattern obtained at $\theta = 25^{o}$. b) LO Optical path scheme for array pumping. This represents the side view of the optical path, with the full pattern being collimated.

The aperture stop works simply by physically blocking the incoming beam by means of a variable aperture diaphragm. Using this element we achieve two things: first a small incoming beam (10 mm diameters was found to yield the best trade off between sufficient intensity and practical beam shape for our FIR gas laser) which is a requirement for the array, and secondly, we were able to obtain a clean beam by allowing through the aperture stop only one of the double peak originating from the gas laser. The final setup achieved can be seen in figure 4.12b. The addition of the beamsplitter allows us to test the beam pattern in real conditions, since this element is crucial to combine the radiation from the LO and the unknown signal. At the same time, it allows us to test different beamsplitter thickness's, which will be a good indicator of

the pumping efficiency since lower thickness means less LO is being reflected into the cryostat. Also, it will mean better sensitivity will be possible to achieve since there is a lower signal loss in thinner beamsplitters.

The only catch with our setup is since only one lens is used, the beams after the grating although ideally parallel in relationship to each other, are at the same time being focused. This is not necessarily a problem, since from the position where the lens gathers the beam pattern until the point the beam pattern comes back to exactly the same size, it takes 100 mm, which is more than enough to work with. There would be a away to solve this, if in our first attempt to collimate the beam pattern, both the lens used to achieve this and the focus lens would be matching lenses (same focal length), but no lenses were available to make this possible.

4.3.2 2x2 Array demonstration

To demonstrate the 2x2 array using the center four beams, a lens was used with a focal length of 50 mm and 40 mm diameter, this was the only suitable lens available. From our results θ=15º would be the optimum in terms of even distribution of the beams. During the experiments however, it was clear that the angle was too low for practical arrangement of the optical apparatus. Therefore we opted to use the grating at an incident angle of 25º which we know to have almost the same efficiency, and also similar central beam pattern. The results of the beam pattern at 10 and 90 mm after the lens are shown respectively in figures 4.13a 4.13c, overlapped on the figures is an outline of the array for reference.

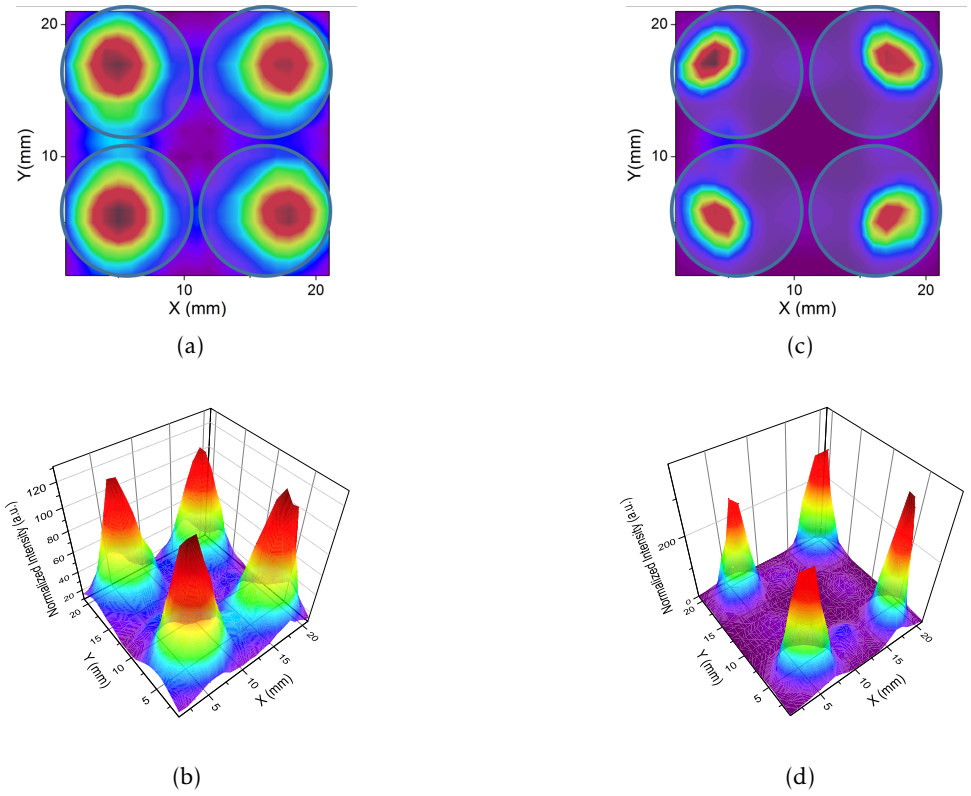

Figure 4.13: a) Beam pattern at 10 mm after the lens. b)3D view of a). c) Beam pattern at 90 mm after the lens. d) 3D view of c). Both a) and c) have the array overlapped for reference. The scale for both images are normalized between each respective minimum and maximum, so no comparison of power should be made based on them.

It was obtained a pitch size between beams of 12 mm, while the expected was 10 mm (based

on the equations deduced in appendix D). This difference can be justified by both lack of resolution as mentioned in the angle calculations, and by the lens not being positioned at the exact correct distance from the grating. This last justification agree with the 3D images of the beam pattern where is possible to see that the beams peaks seems to be still diverging slightly. Although the pitch size being slightly bigger than the array, it is compensated by the spot size of the beams being smaller than the lens. It was expected to have similar beam shapes at both measurements, since they were taken at the same distance from the focus point. What happens in reality is that the beam seems to be suffering some additional focusing effect, hence showing smaller radius at the farthest measurement. It can also bee seen that although the difference in size, the center of the beam remains almost the same, so we assume the beams to be almost collimated. The reason for the beam size disparity can be due to the original beam not being perfectly collimated. Nevertheless, this allowed for more space to maneuver the position of both the beamsplitter and cryostat. In figure 4.14 it can be seen the setup during the testing.

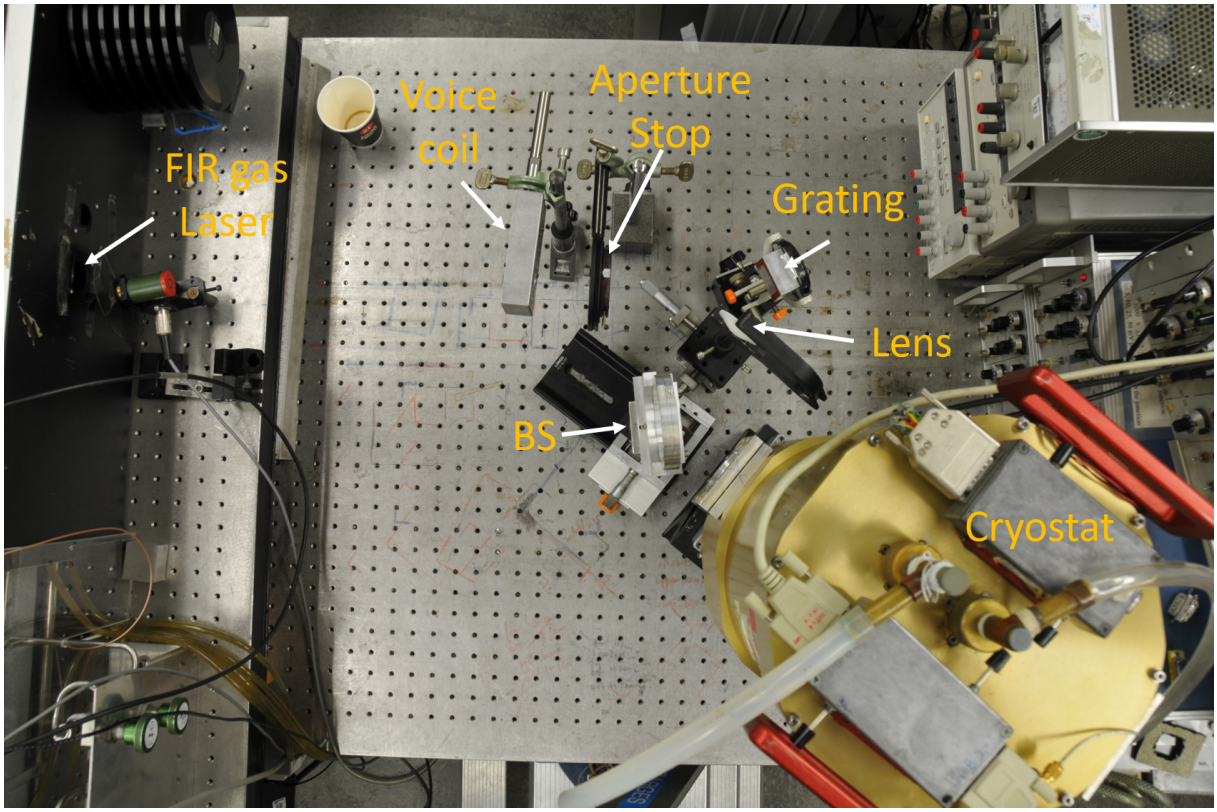

Figure 4.14: Picture of the setup used to pump the array during the grating test. The laser beam comes out of the FIR Gas laser passing through the aperture stop, where the desired beam size is obtained. The beam then illuminates the grating, having the output pattern gathered at the lens. This lens is positioned at a distance (50mm) which match its own f number, allowing to collimate the pattern of the central four beams. The beamsplitter (12 µm thickness, reflects 10% of the radiation from the lens into the cryostat, and simulates where the combination with the astronomical signal will occur.

Finally we tested successfully the four center beams of the grating using a 12 µm beamsplitter, achieving a clear pumped state for all of them at once. The output power of our gas laser is in the order of 1 mW. The results are presented in figures 4.3.2 and 4.3.2. For each of the pixels one can be clearly see the full IV curves (negative part included) for each of the pixels, at

both situations. The figures represent a Labview based oscilloscope which was devised to give simultaneous real-time curves for all four pixels, allowing for easier alignment. The array block was positioned in the cryostat, and each of the HEB connected to its own bias box. All of the bias box were connected to data aquiction board, feeding the information to our work computer, in which data was acquired by the Labview program. It was confirmed that four different beams were in place by blocking the optical path closer to the lens, where the correspondent pixel went dark. This was done for every pixel and a clear response was observed in each corresponding IV curve.

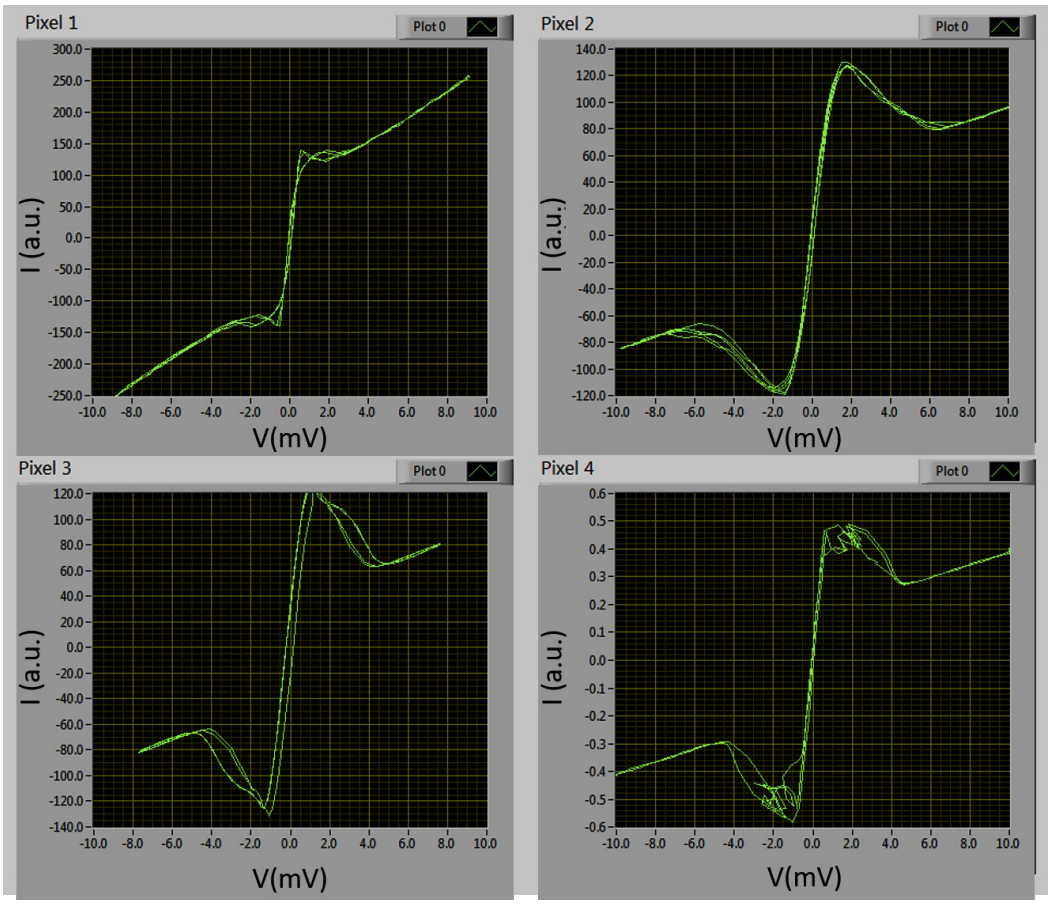

Figure 4.15: Array umpumped IV curves.

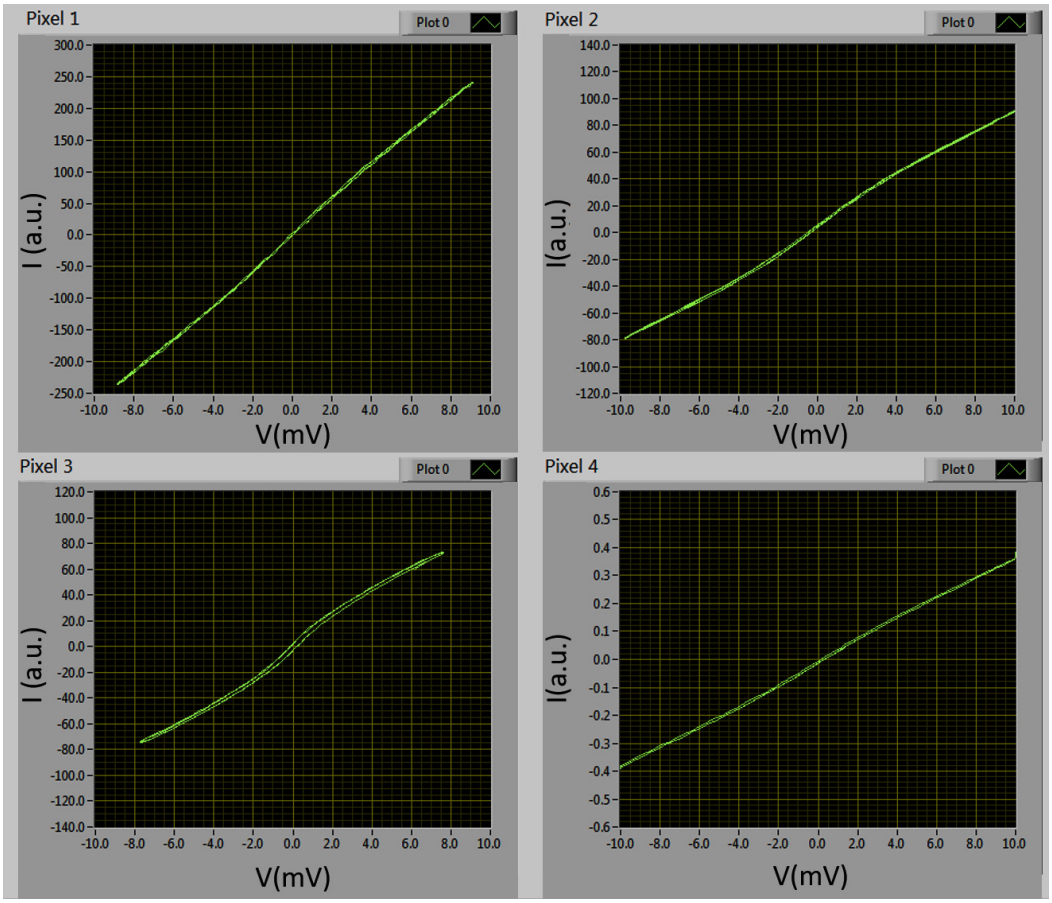

Figure 4.16: Array fully pumped IV curves.

With such promising results we moved onto understand what the requirements would be to make use of all the beams. Assuming that the center four beams of the beam pattern are arranged in a square shape it is possible to derive for any grating, based on its α and β that the pitch size between the center four beams, d_c, and the pitch size between the outer beams and the closest center ones, d_o are:

$$d_c = 2f \times \tan(\alpha) \tag{4.1}$$

$$d_o = 2f \times \tan(\beta) \tag{4.2}$$

Assuming the diagonal of the pattern, it is possible to calculate the diameter of the collimating lens required (the full demonstration can be found in appendix D):

$$D = 2f\sqrt{(\tan^2(\alpha) + \tan^2(\beta))} + Lens_D \tag{4.3}$$

Where $Lens_D$ is the lens diameter used for the array, 10 mm in this case. From here is possible to engineer the lens $F\#$, which is a measure of how fast a lens is. Values below 1 are not desirable since those lenses would be too thick, and therefore induce high LO power losses.

$$F\# = \frac{f}{D} = \frac{f}{2f\sqrt{\tan^2(\alpha) + tan^2(\beta)} + lens_D} \tag{4.4}$$

Using the values of α and β calculated for our grating, the behavior of $F\#$ is plotted in figure 4.17a. Here it can be seen that for any lens with a focal length below 34 mm would always lead to a lens with an $F\#$ below 1. It can be seen that this value starts to increase slower as we move into longer focal lengths. In fact, assuming $f >> lens_D$, we can approximate equation 4.4 to:

$$F\# = \frac{1}{2\sqrt{\tan^2(\alpha) + tan^2(\beta)}} \tag{4.5}$$

From where it can be concluded that the lens $F\#$ is fundamentally limited by the angles of the grating. For the specific case of the grating studied here, the $F\#$ is limited to a maximum of 1.67.

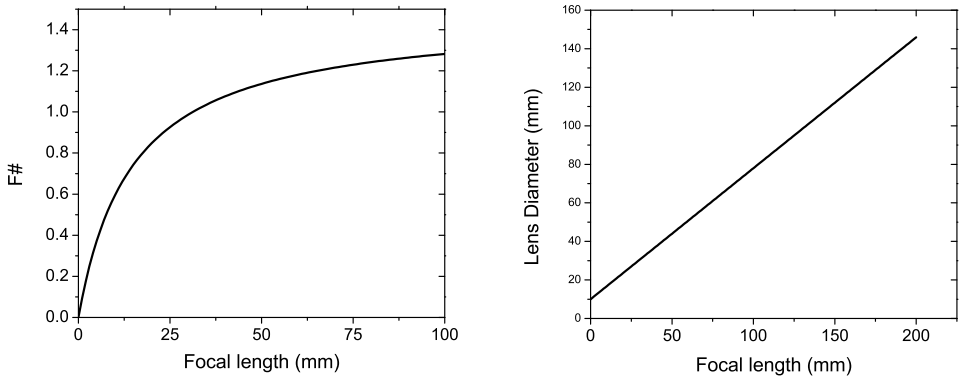

(a) (b)

Figure 4.17: Conditions required to collimate the beam pattern and match it to the array used. a)Lens $F\#$ vs focal length. b) Lens diameter vs the focal length.

Looking at the focal length we where working with, 50 mm, the diameter required to gather all the pattern was 44 mm, so our lens was too small for this. Taking into account the best suitable focal length required to match the grating pattern to our array was theoretically 55 mm, we would need a lens with 50 mm (including some extra margin). It was not possible to have such a specific lens made before the end of this thesis work, and therefore we couldn't demonstrate the full pattern. Based on experience gathered in the demonstration of the 2x2 array, it was expected to have a real pitch size bigger than reality, which would still be compensated by a smaller beam size, and therefore possibly demonstrate the full pattern.

Chapter 5

Conclusion and future perspectives

This thesis summarizes the work towards a 4x2 HEB mixer array at 4.7 THz based on a Fourier phase grating LO. The main goal within the thesis was to check the viability of such an array. For this, different task were set:

1. Characterization of multiples HEB devices in order to understand the possibility of having enough devices with similar characteristics to populate the array;

2. Study how the lens size might influence the noise temperature (sensitivity) of the devices, with the aim of reducing the size of this optical element which would allow for more compact arrays;

3. Study for the first time the optical performance of a 4x2 Fourier phase grating at such high frequency (1.4 THz) with the aim of pinpointing the critical characteristic of such novel element that should be taken into account before moving into the desired 4.7 THz frequency. It was also aimed to demonstrate if possible a 4x2 pumped array using this grating.

On the first task, ten devices were studied from a single batch, NV08, where the noise temperature (T_n) was obtained using the hot/cold Y factor technique and the pumping power (P_{opt}) using the isothermal method, from where it was concluded the following specs at 2.5 THz : $R_N = 64.8 \pm 1.8\,\Omega$, $I_c = 197 \pm 25\,\mu A$, $T_n = 962 \pm 29\,K$ and $P_{opt} = 227 \pm 13\,nW$. The fact all of the devices from this batch show noise temperature much below the GUSTO requirements (1500 K) and that the variation of the parameters is very low, allows to draw the conclusion that we have already the required devices for the array, and that more devices can be drawn from the batch both for this 4.7THz array and for improvements on the 1.4 and 1.9 THz arrays required. Also we conclude that this fabrication batch is very consistent and reliable, since all the device studied, picked at random, were working properly. It is also known based on the noise curves for the mixers, that the pump power can vary with little influence to T_{REC}. Although from 2.5THz to 4.7THz a 30% increase in noise will occur, it will also be used AR coated lens, which will compensate for this effect.

During the lens study, four lenses were compared, a 10 mm lens plus three different designs of 3.1 mm lens. They were originally studied in our vacuum setup using always the same device, picked from the ten characterized from batch NV08. The fist results showed that design 1 (L1) was the best of the 3, although design 2 (L2) had a very similar behavior. The noise difference from the 10 mm to the L1 was approximately 26% (from 973 K to 1230 K). Due to some lack of trust using the smaller lens, another study was performed, to check the difference between the vacuum setup and an air setup, where no geometric misalignment of the loads used for characterization would exist. Here a difference was noticed for the 10 mm and the L1 between vacuum and air. It was expected, if the vacuum system was perfect, for both lenses to have the same behavior moving into air measurements, which didn't happen. The 10 mm increased 28% in noise, while the L1 only increased 17% hence leading to the conclusion that the previous

reported 26% increase noise between 10 mm and L1 is a overestimate of the noise introduced this way. Since our devices on average have 962 K noise temperature, it is expected in the worst case scenario this value to rise to 1212 K, which is still below the requirements. So the conclusion is that smaller lens can be introduced in the future array without significant drop in system noise temperature.

The grating was the most challenging part of all the work, not only because of itself but because of all the required optical elements for its characterization. In the end it was concluded that the grating works fundamentally as a mirror, copying the image of the incident beam into the sub-beams generated. Its key characteristics beside the obvious beam pattern (4x2 beams) are the efficiency, the angle where the more uniform pattern can be achieved, and the angular distribution of the beam, which we defined using two angles α center of one four beam column to the center of the first beam, calculated to be 5.7º and β, the angle obtained between the center of the four beam column and the outer beams, calculated at 18º. For our grating the best pattern was seen at 15º, which also showed the highest total efficiency of 71%. 25º was the expected best incident angle, and the efficiency obtained, 69%, was very close to the one at 15º, but the beam pattern is not as good. Rotation the grating into a 2x4 beam pattern was also studied but proved less useful for practical applications due poor distribuition of power.

Finally it was demonstrated the pumping of a 2x2 HEB mixer array, which had been used in a previous report. For this the central four beams were chosen and engineered in order to obtain small collimating beams which were used to successfully pump the array. Based on the mathematical deductions of the grating beam pattern evolution in distance, it was found that in order to match the beam pattern to our array, having the beam pattern collimated, a lens with focal length of 55 mm and 50 mm diameter could be used. Such lens was not possible to fabricate in time for this work.

The next step would be to have the previously mentioned lens fabricated in order to test if it would allow for the demonstration of the full beam pattern. After this, the goal would be to move into the 4.7 THz grating. This last goal is already in motion but due to delays in the new grating fabrication it was not possible to show any preliminary results on it. This new grating will take into account all the knowledge gathered in the last months and hopefully will be a step forward for arrays. Since batch NV08 showed so promising, more devices should be characterized until 24 devices are available, so all the 3 different arrays expected to fly on GUSTO will have similar characteristics. The 3.1 mm lens study was mainly aimed to study the worst case scenario of lens application, the real goal for the new arrays will be a 5 mm lens. The next step here would be to produce a 5 mm lens and study it, confirming the noise expectations, and if it is so, fabricate enough to produce a 4x2 pixel array. The end goal is in the future to have a functional prototype of the array at 4.7 THz tested not with a FIR gas laser, but with a QCL, like what is planned for the real application.

This thesis work marks the end of the 1.4 THz study of gratings, preceded by the works already referred throughout the report, so we are now bringing all the parts together to publish a scientific paper.

[1] C. Kulesa. "Terahertz Spectroscopy for Astronomy: From Comets to Cosmology". In: *IEEE Transactions on Terahertz Science and Technology* 1.1 (2011), pp. 232–240.

[2] C. K. Walker. "The Interstellar medium (ISM) at terahertz (THz) frequencies". In: *Terahertz Astronomy*. 2016, pp. 1–35.

[3] F Sizov and A Rogalski. "THz detectors". In: 34 (2010), pp. 278–347.

[4] C. K. Walker. "Incoherent Detectors". In: *Terahertz Astronomy*. 2016, pp. 231–259.

[5] K. D. Irwin, S. W. Nam, B. Cabrera, B. Chugg, G. S. Park, R. P. Welty, and J. M. Martinis. "A Self-Biasing Cryogenic Particle Detector Utilizing Electrothermal Feedback and a SQUID Readout". In: *IEEE Transactions on Applied Superconductivity* 5.2 (1995), pp. 2690–2693.

[6] P. Day, H. LeDuc, B. Mazin, A. Vayonakis, and J. Zmuidzinas. "A broadband superconducting detector suitable for use in large arrays". In: *Nature* 425 (2003), pp. 817–821.

[7] R. Köhler, A. Tredicucci, F. Beltram, H. E. Beere, E. H. Linfield, A. G. Davies, D. A. Ritchie, R. C. Iotti, and F. Rossi. "Terahertz semiconductor-heterostructure laser". In: *Nature* 417.6885 (2002), pp. 156–159.

[8] J. L. Kloosterman, D. J. Hayton, Y. Ren, T. Y. Kao, J. N. Hovenier, J. R. Gao, T. M. Klapwijk, Q. Hu, C. K. Walker, and J. L. Reno. "Hot electron bolometer heterodyne receiver with a 4.7-THz quantum cascade laser as a local oscillator". In: *Applied Physics Letters* 102.1 (2013), p. 011123.

[9] C. K. Walker. "THz Coherent Detection Systems". In: *Terahertz Astronomy*. 2016, pp. 159–227.

[10] J. Zmuidzinas. "Coherent detection and SIS mixers". In: *Proc. Far IR, Sub MM and MM Detector Technology Workshop* (2002), pp. 149–154.

[11] P. L. Richards, T. M. Shen, R. E. Harris, and F. L. Lloyd. "Quasiparticle heterodyne mixing in SIS tunnel junctions". In: *Applied Physics Letters* 34.5 (1979), pp. 345–347.

[12] G. J. Dolan, T. G. Phillips, and D. P. Woody. "Low-noise 115-GHz mixing in superconducting oxide-barrier tunnel junctions". In: *Applied Physics Letters* 34.5 (1979), pp. 347–349.

[13] T. G. Phillips and K. B. Jefferts. "A low temperature bolometer heterodyne receiver for millimeter wave astronomy". In: *Review of Scientific Instruments* 44.8 (1973), pp. 1009–1014.

[14] E. Gershenzon, G. Gol'tsman, I. Gogidze, Y. Gousev, A. Elant'ev, B. Karasik, and A. Semenov. "Millimeter and submillimeter range mixer based on electron heating of superconducting films in the resistive state". In: *Superconductivity* 3.10 (1990), pp. 1582–1597.

[15] D. T. Young and J. C. Irvin. "Millimeter Frequency Conversion Using Au-n-Type GaAs Schottky Barrier Epitaxial Diodes with a Novel Contacting Technique". In: *Proceedings of the IEEE* 53.12 (1965), pp. 2130–2131.

[16] J. R. Gao, M Hajenius, Z. Q. Yang, J. J. A. Baselmans, P Khosropanah, R Barends, and T. M. Klapwijk. "Terahertz Superconducting Hot Electron Bolometer Heterodyne Receivers". In: *IEEE Transactions on Applied Superconductivity* 17.2 (2007), pp. 252–258.

[17] D. E. Prober. "Superconducting terahertz mixer using a transition - edge microbolometer". In: *Applied Physics A: Solids and Surfaces* 62.17 (1993), pp. 2119–2121.

[18] D. J. Hayton, J. L. Kloosterman, Y. Ren, T. Y. Kao, J. R. Gao, T. M. Klapwijk, Q. Hu, C. K. Walker, and J. L. Reno. "A 4.7 THz Heterodyne Receiver for a Balloon Borne Telescope". In: *SPIE , Millimeter, Submillimeter, and Far-Infrared Detectors and Instrumentation of Astronomy VII*. Vol. 9153. 2014, 91531R.

[19] C. Risacher et al. "The upGREAT heterodyne array receivers for far Infrared astronomy". In: *International Conference on Infrared, Millimeter, and Terahertz Waves, IRMMW-THz* (2014), pp. 5–6.

[20] C Groppi, C Walker, and C Kulesa. "Heterodyne Array Development at the University of Arizona". In: *Proc. 14th International Symposium on Space Terahertz Technology*. 2001, pp. 189–203.

[21] D Rabanus, U. U. Graf, S Heyminck, S Stanko, J Stutzki, and I. P.I. D. Universit. "Techniques for Heterodyne Array Receivers". In: *Proc. Far-IR, Sub-MM, and MM Detector Technology Workshop*. October. 2002, pp. 3–6.

[22] J. A. Murphy, C. O. Sullivan, N. Trappe, W. Lanigan, R. Colgan, and S. Withington. "Modal analysis of the quasi-optical performance of phase gratings". In: *International Journal of Infrared and Millimeter Waves* 20.8 (1999), pp. 1469–1486.

[23] U. Graf and S. Heyminck. "Fourier gratings as submillimeter beam splitters". In: *IEEE Transactions on Antennas and Propagation* 49.4 (2001), pp. 542–546.

[24] Y. Luo. "Demonstrating a Fourier phase grating for a terahertz multi-beam local oscillator by". MA Thesis. Delft University of Technology, 2014.

[25] Y. C. Luo, X. X. Liu, D. J. Hayton, L Wei, J. R. Gao, and C Groppi. "Fourier phase grating for THz multi-beam local oscillators". In: *Proc. 26th International Symposium on Space Terahertz Technology*. Vol. 1. Cambridge, 2015, pp. 25–26.

[26] X. Liu. "Demonstration of 2 x 2 heterodyne receiver array at 1.4THz using HEB mixers and Fourier phase grating LO". MA Thesis. TUDelft, 2015.

[27] X. X. Liu, D. J. Hayton, Y. C. Luo, L Wei, N. V.J. R. Gao, and C Groppi. "A 2 x 2 Array Receiver at 1.4 THz based on HEB mixers and a Fourier Phase Grating Local Oscillator". In: *Proc. 26th International Symposium on Space Terahertz Technology*. Cambridge, 2015, pp. 16–18.

[28] A. R Kerr, M. J Feldman, and S. Pan. "Receiver Noise Temperature, the Quantum Noise Limit, and the Role of the Zero-Point Fluctuations *". In: *8th Int. Symp. on Space Terahertz Tech*. 304. 1997, pp. 101–111.

[29] W. Zhang, P. Khosropanah, J. R. Gao, E. L. Kollberg, K. S. Yngvesson, T. Bansal, R. Barends, and T. M. Klapwijk. "Quantum noise in a terahertz hot electron bolometer mixer". In: *Applied Physics Letters* 96.11 (2010), pp. 11–13.

[30] H. Ekström, B. S. Karasik, E. L. Kollberg, and K. S. Yngvesson. "Conversion Gain and Noise of Niobium Superconducting Hot-Electron-Mixers". In: *IEEE Transactions on Microwave Theory and Techniques* 43.4 (1995), pp. 938–947.

[31] R. Farinha. "Modelling of a lens antenna receiver system for NASA GUSTO". MA Thesis. Faculty of Science and Technologies, New University of Lisbon, 2016.

[32] U. U. Graf, S Heyminck, E. A. Michael, S Stanko, C. E. Honingh, K Jacobs, R Schieder, J Stutzki, and B Vowinkel. "SMART: The KOSMA sub-millimeter array receiver for two frequencies". In: *Millimeter and Submillimeter Detectors for Astronomy*. 2003, pp. 322–329.

[33] K.-F. Schuster, J. Blondell, Y. Bortolotti, M. Carter, B. Fouilleux, B. Lazareff, F. Mattiocco, F. Morel, A. Perrigouard, and J.-L. Pollet. "The IRAM 230 GHz Multibeam SIS Receiver". In: *Eight International Symposium on Space Terahertz Technology*. March. 1997, pp. 499–504.

[34] C Kasemann and Others. "CHAMP+: A powerful submm Heterodyne Array". In: *Proc. 19th International Symposium on Space Terahterz Technology*. April. 2008, pp. 166–172.

[35] T de Graauw and F Helmich. "Herschel-Hifi: The heterodyne instrument for the far-infrared". In: *Proc. Symposion "The Promise of the Herschel Space Observatory"*. July. 2001, pp. 45–51.

[36] C. Walker, C. Kulesa, and C. Groppi. "The Stratospheric Terahertz Observatory (STO)". In: *Proc. 19th International Symposium on Space Terahertz Technology*. April. 2008, pp. 28–30.

Appendix A

State of the art

Table A.1: Summary of the state of the art on heterodyne instruments

Instrument/ /Platform	Front-end	Frequency	LO multiplexing Scheme
PolarStar/ Astro telescope [20]	4 SIS mixer array Quasi -Optic	810 GHz	Two low loss beam splitters
DesertStar/ Heinrich Hertz telescope [20]	7 SIS mixer array Hexagonal shaped (Quasi-optic)	345 GHz	Phase Grating
SMART/ KOSMA telescope [32]	2x4 SIS mixers (Quasi-optic)	490/810 GHz	Collimating Fourier Grating
HERA/IRA telescope [33]	9 (3x3) SIS mixer array (Quasi-optic)	230 GHz	3 way waveguide power splitter
CHAMP/ ALMA [34]	2x7 SIS mixer array Hexagonal shaped (Quasi-optic)	690/810 GHz	Collimating Fourier Grating
HIFI/ Herschel [35]	1x7: SIS 1x7: HEB	1250 GHz 1.4/1.9 THz	Waveguide Power Splitter
STO-2 observatory [18, 36]	2x4 HEB mixer array +Single Pixel (Waveguided based)	1.4/1.9/ 4.7 THz	Waveguide power Splitter
upGreat/ SOFIA [19]	2x7 HEB mixer array 1x7 HEB mixer array	1.9-2.5/ /4.7 THz	Waveguide power splitter (under development)
GUSTO	3x8 HEB mixer array	1.4/1.9/ /4.7 THz	Waveguide power splitter; Fourier Phase Grating at 4.7 THz (under development)

GUSTO Mission

GUSTO[1] is a candidate balloon mission from NASA which will launch a high-altitude balloon with a one-meter telescope. The aim is to provide a comprehensive understanding of the inner workings of our galaxy and one of our companion galaxies, the Large Magellanic Cloud (LMC), by tracing all phases of the interstellar medium. In that respect GUSTO is complementary to the European Herschel space telescope (ESA, 2009-2013), and the Japanese SPICA telescope (JAXA).

NASA has recently selected five Explorer Mission Program of Opportunity proposals for a Phase A-Concept Study. GUSTO, which stands for Galactic/X-galactic Ultra long duration balloon Spectroscopic Stratospheric THz Observatory, is one of two astrophysics missions selected. Of these two missions NASA plans to choose one for flight. SRON and the Kavli Institute of Nanoscience of the TU Delft will provide the key detector technology for GUSTO's 4.7 THz camera.

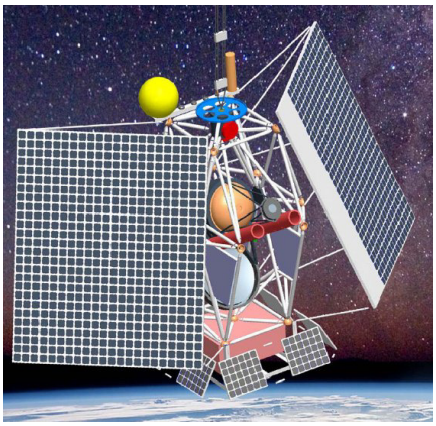

Figure B.1: Illustration of the GUSTO balloon.

The balloon will be launched from Williams Field, the Antarctic. During its 100 day flight it will spiral out from the Antarctic circling the Earth. As it drifts northward more and more of the Milky Way will become visible, allowing a large scale survey to be performed. At its flight altitude of 36 km there is only a trace amount of water vapor , the primary source of absorption at THz frequencies. Therefore the observing conditions are nearly the same as in space. As of the last update (2016), NASA will be deciding in April 2017 which project to sponsor, being expected GUSTO to fly in 2020.

The work at SRON has been financially supported by different funding agencies such as ESA, EU FP7, NWO, and KNAW. The last two are supporting a joint research activity between The Netherlands (SRON-TUDelft) and China (Purple Mountain Observatory) and play a crucial role for the most recent development.

All the information here was taken from https://www.sron.nl/missions-gussto. Some corrections were made based on current project updates. No more information can be disclosed at this point, since it is waiting for NASA funding.

[1] The name was changed recently from GUSTO

Appendix C

Instruments used

Table C.1: Summary of the instruments used in the entire work.

Function	Instrument
Gas Laser	FIR gas laser
PID controller (voice coil)	Stanford Research Systems SIM 960 Analog PID controller
Power meter	Agilent E4418B Single Channel power meter
Bias suplies	Bias supply box made by SRON
Power Sensor (Reference)	Agilent E4412 CW diode power sensor
Power Sensor (Measurements)	Agilent E4418B
Raster Scan	Newport XPS

Grating equations demonstration

To demonstrate how to dimension an array and the lens required to match the beam pattern of the grating, we first should analyze the side view of the beam pattern (see figure D).

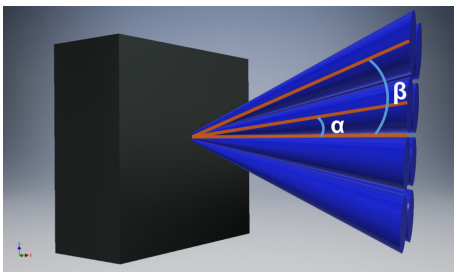

Figure D.1: 3D simulation of the grating beam pattern. Flat plan intersection. Representation of the side angles.

The angles equations can be quickly extracted:

$$\alpha = \arctan(s1/d) \tag{D.1}$$

$$\beta = \arctan(s2/d) \tag{D.2}$$

The distance, d, is the distance between the grating and the plane of interest (e.g. the scanning plane in the grating characterization), but it can be also understood as the focal length, f, of the lens required to collimate the beam pattern. s1 and s2 are the distance from the center of the image to the center of the closest and farthest beam respectively, in the same column. They also represent the half pitch distance between the central beams, and the outer beams, respectively d_c and d_o. Based on equations (D.1) and (D.2) it can obtained:

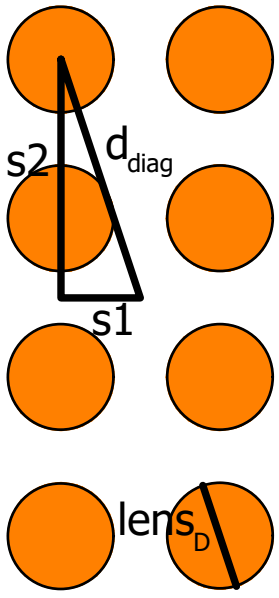

Figure D.2: Ideal beam pattern. Representation of the different distances considered.

$$d_c = 2f \times \tan(\alpha) \tag{D.3}$$

$$d_o = 2f \times \tan(\beta) \tag{D.4}$$

This equations can be used to dimension an array that can best match our grating beam pattern. The lens required to collimate the beam pattern need to have a diameter, D, capable of gather all the radiation. Looking at the scheme of the ideal beam pattern in figure D.2, the diameter can be seen as two times the distance between the center of the pattern to the center of one of the outer beams,d_{diag}, plus the lens diameter used in the array (assuming the beams diameter is the same of the lens), $lens_D$:

$$D = 2d_{diag} + lens_D \tag{D.5}$$

Assuming the central four beams form a perfect square. The diagonal of the pattern can be calculated using the Pitagoras theorem:

$$(d_{diag})^2 = \left(\frac{d_c}{2}\right)^2 + \left(\frac{d_o}{2}\right)^2 \tag{D.6}$$

Substituting in equation (D.6) the expressions derived in (D.3) and (D.4):

$$d_{diag}^2 = (f \times \tan(\alpha))^2 + (f \times \tan(\beta))^2 \tag{D.7}$$

and finally

$$d_{diag} = f\sqrt{(\tan^2(\alpha) + tan^2(\beta))} \tag{D.8}$$

Substituting equation D.9 in (D.5, D is easily obtained:

$$D = 2f\sqrt{\tan^2(\alpha) + tan^2(\beta)} + lens_D \tag{D.9}$$

Having this is now easy to obtain the $f\#$ of any lens that can collimate our pattern, as function of f.

$$F\# = \frac{f}{D} \tag{D.10}$$

$$F\# = \frac{f}{2f\sqrt{\tan^2(\alpha) + tan^2(\beta)} + lens_D} \tag{D.11}$$

If $f >> lens_D$, then equation D.11 is approximately:

$$F\# = \frac{1}{2\sqrt{\tan^2(\alpha) + tan^2(\beta)}} \tag{D.12}$$

So the lens $F\#$ is fundamentally limited by the angles of the grating.